JEM Journal of Experimental Medicine

ARTICLE

Vasculature-associated fat macrophages readily adapt to inflammatory and metabolic challenges

Hernandez Moura Silva[1], André Báfica[1,2,3], Gabriela Flavia Rodrigues-Luiz[2], Jingyi Chi[4], Patricia d'Emery Alves Santos[1], Bernardo S. Reis[3], David P. Hoytema van Konijnenburg[3], Audrey Crane[4], Raquel Duque Nascimento Arifa[1], Patricia Martin[1], Daniel Augusto G.B. Mendes[2], Daniel Santos Mansur[2], Victor J. Torres[5], Ken Cadwell[1,5], Paul Cohen[4], Daniel Mucida[3], and Juan J. Lafaille[1,6]

Tissue-resident macrophages are the most abundant immune cell population in healthy adipose tissue. Adipose tissue macrophages (ATMs) change during metabolic stress and are thought to contribute to metabolic syndrome. Here, we studied ATM subpopulations in steady state and in response to nutritional and infectious challenges. We found that tissue-resident macrophages from healthy epididymal white adipose tissue (eWAT) tightly associate with blood vessels, displaying very high endocytic capacity. We refer to these cells as vasculature-associated ATMs (VAMs). Chronic high-fat diet (HFD) results in the accumulation of a monocyte-derived CD11c$^+$CD64$^+$ double-positive (DP) macrophage eWAT population with a predominant anti-inflammatory/detoxifying gene profile, but reduced endocytic function. In contrast, fasting rapidly and reversibly leads to VAM depletion, while acute inflammatory stress induced by pathogens transiently depletes VAMs and simultaneously boosts DP macrophage accumulation. Our results indicate that ATM populations dynamically adapt to metabolic stress and inflammation, suggesting an important role for these cells in maintaining tissue homeostasis.

Introduction

The adipose tissue of healthy animals contains a large population of innate and adaptive immune cells, numerically dominated by macrophages (Weisberg et al., 2003; Xu et al., 2003; Lumeng et al., 2007). The functions of these cells in the healthy adipose tissue of animals in steady state are not completely understood. The proportions and numbers of these immune cell types are known to change extensively in conditions such as diet-induced obesity (DIO), genetically determined obesity, and aging, among other situations.

It has been long known that obesity is associated with a heightened inflammatory condition, in which TNFα is an important mediator of insulin resistance (Feinstein et al., 1993; Hotamisligil et al., 1993, 1995). It has been postulated that the myeloid cells found in the adipose tissue during DIO contribute to the pathogenesis of insulin resistance and the metabolic syndrome by increasing their secretion of proinflammatory cytokines (Dalmas et al., 2011; Lumeng, 2013; Wynn et al., 2013; Xu et al., 2013; Fitzgibbons and Czech, 2016; Alemán et al., 2017).

High-fat diet (HFD) induces obesity and insulin resistance in B6 mice (Surwit et al., 1988; Rebuffé-Scrive et al., 1993). Adipocytes become hypertrophic, which could be the initial signal to trigger inflammation (Sun et al., 2011; Rutkowski et al., 2015); however, cultured adipocytes made hypertrophic with oleic acid display insulin resistance without triggering an inflammatory response (Kim et al., 2015). Thus, the role of the inflammatory response in obesity-related disease is not clearly established. Moreover, wild animals endure fluctuations in food supply, in which the adipose tissue triglyceride reserves are mobilized via lipolysis or built from the diet, and little is known about the response of immune cells to these fluctuations.

In this report, we found that tissue-resident macrophages from healthy epididymal white adipose tissue (eWAT), a visceral fat depot, not only surround adipocytes but also associate tightly with blood vessels, being among the most endocytic cells in the body for blood-borne macromolecules. We refer to these macrophages as vasculature-associated adipose tissue macrophages (VAMs). Upon chronic HFD feeding, a monocyte-derived CD11c$^+$CD64$^+$ double-positive (DP) population of macrophages, poorly represented in animals fed a normal diet (ND), surges in the eWAT. Contrary to some predictions, these macrophages

---

[1]Kimmel Center for Biology and Medicine at the Skirball Institute, New York University School of Medicine, New York, NY; [2]Laboratório de Imunobiologia, Departamento de Microbiologia, Imunologia e Parasitologia, Centro de Ciências Biológicas, Universidade Federal de Santa Catarina, Florianópolis, Santa Catarina, Brazil; [3]Laboratory of Mucosal Immunology, The Rockefeller University, New York, NY; [4]Laboratory of Molecular Metabolism, The Rockefeller University, New York, NY; [5]Department of Microbiology, New York University School of Medicine, New York, NY; [6]Department of Pathology, New York University School of Medicine, New York, NY.

Correspondence to Juan J. Lafaille: juan.lafaille@med.nyu.edu; Hernandez Moura Silva: hernandez.mourasilva@med.nyu.edu.

Rockefeller University Press

https://doi.org/10.1084/jem.20181049

J. Exp. Med. 2019 Vol. 216 No. 4 786–806

have predominantly an anti-inflammatory and repair gene signature. Importantly, eWAT macrophages from HFD-fed mice have a reduced endocytic capacity. Differently, a brief fasting period rapidly and reversibly reduces all macrophage populations, especially VAMs. Acute systemic inflammatory stress, such as that induced by LPS administration or *Salmonella enterica* serovar Typhimurium infection, results in a rapid and transient reduction in the main populations of VAMs; however, in this case, the decrease in VAMs is accompanied by an increase in DP macrophages. Taken all together, the macrophage populations dynamically adapt to metabolic stress and inflammation by adjusting their numbers and the expression of beneficial genes, even when pathology ends up prevailing.

Results

WAT in steady state has multiple populations of macrophages

We characterized the eWAT lymphoid and myeloid cell populations under steady state. We chose to focus on the visceral WAT because excess abdominal fat, unlike excess subcutaneous fat, strongly correlates with metabolic syndrome (Sharma, 2002; von Eyben et al., 2003). First, we performed an extensive flow cytometry analysis in perfused adult male mice. Flow cytometry of adipose tissue macrophages (ATMs) is made somewhat difficult because of their high autofluorescence. To minimize the impact of autofluorescence, we carefully selected the fluorochromes for each cell marker and used fluorescence minus one controls (FMOs). The gating strategy, including all markers, is shown in Fig. S1 (A–H), and the abbreviated list of surface markers used throughout this article to identify the key myeloid populations is shown in Fig. 1 A. The expression of a series of commonly used surface markers for the eWAT myeloid populations is shown in Fig. S1 I. We observed a minor Ly6C^{HIGH} monocyte population (Fig. S1 G), the two main populations of dendritic cells (DCs), CD11b$^-$ (Fig. S1 E) and CD11b$^+$ (Fig. S1 H), and four populations of macrophages, besides eosinophils (Fig. S1 F), neutrophils (Fig. S1 F), innate lymphoid cells, and lymphocytes. As rationalized below, we refer to the macrophage populations as VAM1, VAM2, PreVAMs, and DP macrophages (Fig. S1, D and H). VAM1 and 2 are similar but can be readily distinguished by their surface expression level of MHCII and Tim4 (Fig. S1 D). To gain information regarding cell morphology, we sorted the populations and observed them in Giemsa-stained cytospin preparations. The most remarkable aspect is that, in healthy mice eating an ND, VAMs and PreVAMs have lipid droplets in their cytoplasm (Fig. S1 J), a morphology that resembles ATMs from obese mice (Aouadi et al., 2014), but, to our knowledge, have not been previously reported in adipose macrophages from lean mice. The composition of all immune cells in the healthy male eWAT is summarized in Fig. S1 K. The combination of the two VAM populations outnumbers the sum of all other CD45$^+$ eWAT cells. CD11b$^+$ DC and eosinophils are, respectively, the third and fourth cell types by abundance. DP macrophages, which are quite rare in eWAT from mice fed ND (Fig. S1 K), express high surface levels of CD11b, CD11c, CD64, and MHCII and intermediate levels of CD206. We refer to these macrophages as DP because of their surface expression of both CD11c and CD64. PreVAMs and DP macrophages express lower level of surface CD206 than VAMs (Fig. S1 I). Thus, the myeloid populations that form the eWAT are more complex than previously described. To summarize the eWAT hematopoietic composition in a visual manner, we performed t-distributed stochastic neighbor embedding (t-SNE) analysis for CD45$^+$ and CD11b$^+$SiglecF$^-$Ly6G$^-$ eWAT cells (Fig. 1, B and C).

Given this complexity, we further used RNA sequencing (RNASeq) to analyze the transcriptome of purified eWAT monocytes, macrophages, and DCs. Principal component analysis (PCA) showed that VAM1, VAM2, and PreVAMs cluster near each other (Fig. 1 D). CD11b$^-$ DCs and eWAT monocytes are more distant from the other myeloid cells analyzed. An unbiased global heat map illustrates the similarities and differences between the eWAT cell types studied (Fig. 1 E). The assessment of key transcription factor expression corroborates the existence of three major groups, one containing VAM1, VAM2, and PreVAMs; another containing the two DC populations; and the other containing monocytes and DP macrophages (Fig. 1 F).

eWAT monocytes rapidly acquire an adipose tissue signature but do not generate VAMs under steady state

We identified a small population of cells expressing Ly6C^{HIGH}, CD11b$^+$, CD115$^+$, CD64$^+$, MHCII$^-$, NK1.1$^-$, Ly6G$^-$, SiglecF$^-$, and CD206$^-$, which are markers used to identify Ly6C^{HIGH} monocytes (Mildner et al., 2017). However, unbiased gene expression analysis indicated that these eWAT monocytes were quite distinct from the main blood monocyte populations, Ly6C^{HIGH} or Ly6C^{LOW} (Fig. 2 A), as confirmed by PCAs and volcano plots (Fig. 2, B–E). To assess the kinetics of monocytes in the eWAT, we injected BrdU and chased the labeled cells. By 72 h, the BrdU label was becoming undetectable, a consequence of replacement with new incoming precursors, which are unlabeled, and of dilution of the BrdU$^+$ label by cell division. We could observe a peak of BrdU labeling in the eWAT monocytes at 24 h, followed by a decline (Fig. 2 F). Thus, the process of eWAT monocyte differentiation appears to be rapid.

To further study the origin of eWAT myeloid cells, we performed a genetic fate mapping experiment using *Cx3cr1*$^{Cre\text{-}ERT2\text{-}EYFP}$ × *Rosa26*$^{LSL\text{-}DsRed}$ mice (Parkhurst et al., 2013), in which tamoxifen was administered to label with DsRed all cells expressing CX3CR1 at the time of administration, such as eWAT monocytes (Fig. S1 I), monocyte-DC precursors (MDPs), and common DC precursors (http://www.immgen.org). Microglia were used as a positive control because of their robust labeling by this method (Parkhurst et al., 2013; Wolf et al., 2017). There was a peak of DsRed on eWAT monocytes on day 5 after tamoxifen administration, with the label being greatly reduced by day 10 (Fig. 2 G). This result indicates that DsRed$^-$ precursors, such as hematopoietic stem cells, differentiate into eWAT Ly6C^{HIGH} monocytes and replenish the majority of the eWAT monocyte compartment in as little as 10 d. In addition, by day 10, DsRed$^+$ eWAT monocytes either differentiated into another cell type or died. The kinetics of PreVAM labeling, with a peak at day 10, is compatible with the first possibility. VAMs do not express sufficiently high CX3CR1 levels (Fig. S1 L) to induce DsRed expression upon tamoxifen administration, and they acquire only a minimal DsRed labeling at late time points, further indicating

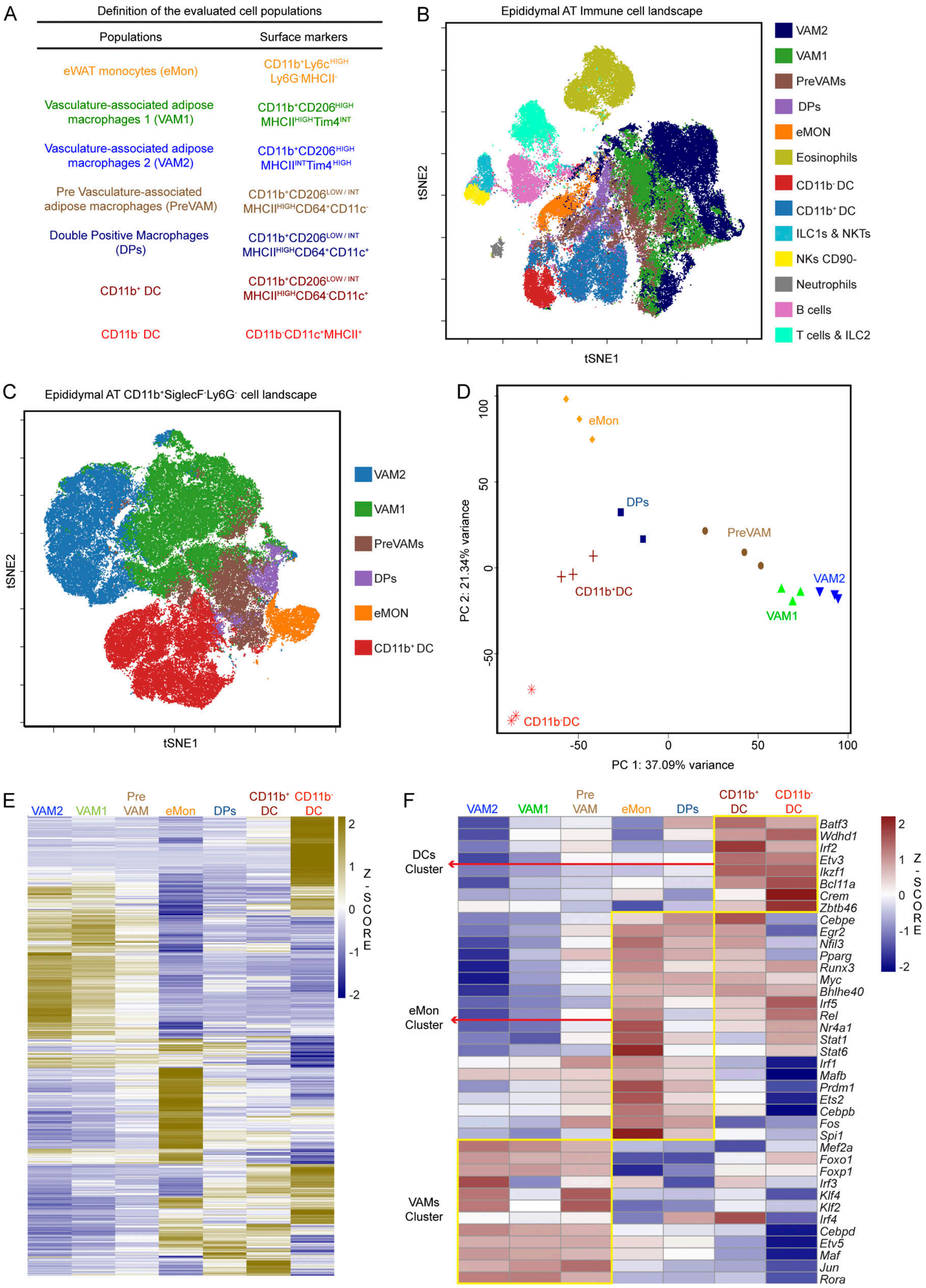

Figure 1. **eWAT harbors a complex distribution of immune cells containing four macrophage subpopulations. (A)** Abbreviated description of the key surface markers defining the cell populations analyzed. The colors identifying each population are used throughout the manuscript. **(B)** t-SNE map displaying the distribution of 200,000 CD45$^+$ cells from the eWAT of steady state WT mice, analyzed by flow cytometry. Colors correspond to Cytobank-guided clustering of cell populations. Representative plot of three independent experiments (*n* = 3). **(C)** t-SNE map displaying the distribution of 100,000 CD45$^+$CD11b$^+$CD90$^-$CD19$^-$Ly6G$^-$SiglecF$^-$ cells from the eWAT of steady state WT mice analyzed by flow cytometry. Colors correspond to Cytobank-guided clustering of cell populations. Representative plot of three independent experiments (*n* = 3). **(D)** PCA of the transcriptional signature obtained by RNAseq data from the

populations described in A. Adult (average 16-wk-old) WT males were used. Each dot represents data from a pool of two to three epididymal fat pads. **(E)** Unbiased gene expression profile of eWAT myeloid subpopulations described in A, showing all genes for broad visualization. Each column represents consolidated data from three biological replicates per cell type. The z-score of the gene expression profiles gives a scale to measure the differential expression. **(F)** Heat map of transcription factors differentially expressed among eWAT myeloid subpopulation. The yellow boxes depict clusters of transcription factors predominantly expressed by DCs (DC cluster), monocytes (eMon cluster), and VAMs (VAM cluster) in the eWAT in homeostasis. Each column represents consolidated data from three biological replicates. The z-score of the gene expression profiles gives a scale to measure the differential expression. Adult (average 16-wk-old, range 12–20) WT males were used.

that they do not normally differentiate from DsRed$^+$ cells such as monocytes or MDPs.

Finally, to study the repopulation of eWAT myeloid cells from bone marrow precursors, we irradiated WT CD45.1$^+$ mice only in the hind legs and reconstituted the irradiated mice with CD45.2$^+$ bone marrow. Under these conditions, the eWAT, most of the bone marrow, the brain, and all viscera are protected from irradiation, but the hind legs' exposure allows some level of chimerism. After 2 mo, we analyzed the donor-derived CD45.2$^+$ cells. Virtually all myeloid populations in the eWAT were similarly reconstituted to the level observed for blood Ly6C^{HIGH} monocytes (5–10%) by bone marrow progenitors, with the clear exceptions of VAM1 and, especially, VAM2 (Fig. 2 H). These data are in agreement with a study showing that ATMs proliferate locally (Amano et al., 2014). Since VAMs are the most abundant eWAT macrophages, studies addressing all ATMs are likely to detect mostly their properties. Adipose monocytes, DP macrophages, and PreVAMs were, as anticipated, predominantly bone marrow derived.

In conclusion, our data indicate that once monocytes enter the eWAT, they rapidly begin to acquire a unique gene expression profile, while transiently retaining a monocyte signature. Under normal conditions, they inefficiently generate VAMs. However, as we will discuss in more detail below, monocytes generate DP macrophages and PreVAMs.

VAMs are intimately associated with blood vessels and highly endocytic

Our gene expression analysis suggests that steady state VAM1 and VAM2 macrophages in mice fed an ND have anti-inflammatory, insulin-sensitizing, repair, and detoxifying functions (Fig. 3 A). Confirming and expanding the flow cytometry data, they express high levels of genes encoding the lectin and scavenger receptors, and also genes encoding receptors for “eat me” signals in apoptotic cells (Fig. 3 A).

Unbiased analysis comparing VAM2 with the most abundant nonmacrophage myeloid cell type in the same fat pads, the CD11b$^+$ DCs, showed that VAMs appear to be well equipped for endocytosis in steady state conditions (Fig. 3, B and C). They express high levels of the genes encoding clathrin heavy and α light chain (*Cltc* and *Clta*), the clathrin adaptor protein *Dab2*, and components of the clathrin-associated Ap2 complex, such as *Ap2a2* and *Ap2b1*. Another endocytosis adaptor highly expressed by VAMs was *Eps15*, which has been implicated in both clathrin-dependent and -independent endocytosis (Carbone et al., 1997; Sigismund et al., 2005; Fig. 3 B). Interestingly, VAMs also express high levels of Endophilin B1 (*Sh3glb1*), involved in ultrafast, clathrin-independent endocytosis, a mechanism used by very active cells (Watanabe and Boucrot, 2017). Genes involved in macrophage macropinocytosis, such as *Snx5* and *Snx2* (Lim et al., 2015), are also very highly expressed by VAMs (Fig. 3 B; Kvainickas et al., 2017; Simonetti et al., 2017).

Functional enrichment analysis (gene ontology term analysis) strongly suggests that steady state VAMs have an active endocytic and filtering function (Fig. 3 C). Given the gene ontology indications, we tested the hypothesis that VAMs may be particularly apt at endocytosis of blood substances. First, we observed by confocal microscopy that VAMs maintain close contact with blood vessels, rounding them tightly (Fig. 3 D). To directly test the endocytic capacity, we injected dextran-rhodamine 70 kD i.v., and only 20 min after the i.v. injection, we sacrificed the mice for flow cytometry analysis. VAM1 and VAM2 took up dextran very efficiently, followed by PreVAMs. Neither of the two eWAT DC populations, or the eosinophils, significantly associated with dextran sulfate under these conditions (Fig. 3, E and F). Strikingly, eWAT VAMs took up more dextran-rhodamine than spleen marginal zone macrophages (Fig. 3, E and F). This indicates a special property of eWAT VAMs. Intravital microscopy showed the extremely rapid (5-min) uptake of the i.v.-injected dextran-rhodamine (Video 1 and Fig. 3 G). To confirm that the uptake of dextran-rhodamine by VAMs was not an aberrant result, we injected i.v. a different type of molecule, the protein ovalbumin (Ova). Once again, VAM1 and VAM2 strongly took up fluorescently-tagged Ova, to a higher degree than splenic marginal zone macrophages (Fig. 3 H). This association between Ova and VAMs involved endocytosis and protein processing in vivo, as proven by the fact that VAMs fed in vivo with whole Ova were able to stimulate OTII T cells in vitro (Fig. S2).

To quantify the association between VAMs and vasculature and to visualize the degree of uniformity of VAM distribution throughout the entire fat pad, we used Adipoclear, a whole adipose 3D immunolabeling and clearing method (Chi et al., 2018). To label VAMs, we injected dextran-rhodamine i.v., and 1 h later, we dissected the epididymal fat pad for tissue clearing and whole-mount imaging with a light sheet fluorescence microscope after labeling the vasculature with anti-CD31. VAMs displayed a strong and uniform perivascular localization throughout the entire pad (Video 2 and Fig. 3 I). After the analysis of 300 stacks containing 2,234 macrophages, we concluded that 90.2% of the dextran$^+$ macrophages were in contact with vessels (as analyzed by Imaris software), and <1% of macrophages were at a distance >10 µm (Fig. 3 J). These results show that VAMs are indeed strongly associated with the adipose tissue vasculature. Finally, bodipy labeling of adipose droplets confirmed their presence in VAMs of lean mice (Video 3 and Fig. 3 K). This video further shows the intimate association of VAMs with the vasculature, supporting the use of the VAM nomenclature.

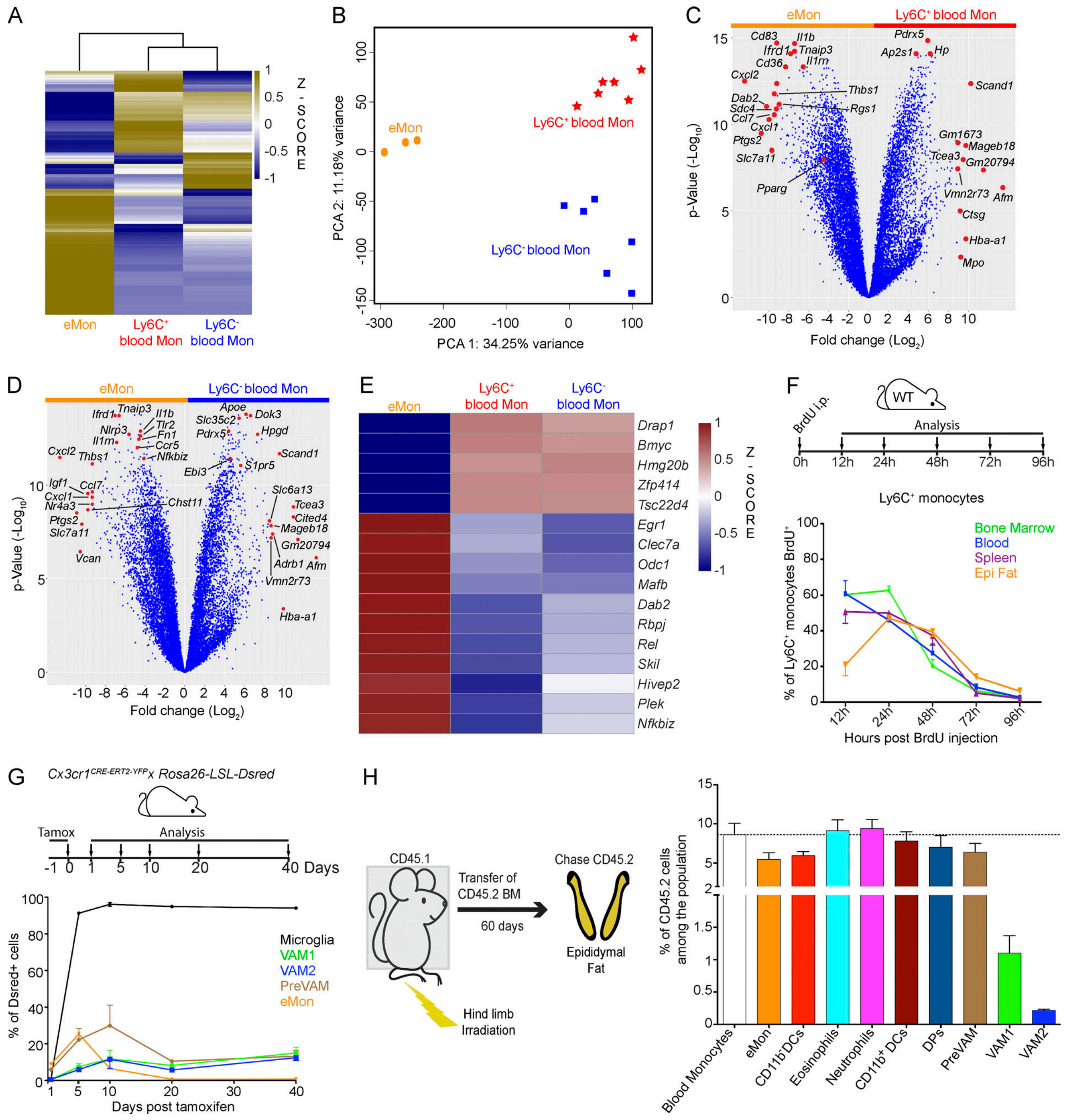

Figure 2. **eWAT monocytes (eMon) rapidly adapt to the adipose tissue environment. (A)** Comparative analysis of eWAT monocyte gene expression compared with blood Ly6C⁺ and Ly6C⁻ monocytes. eMon RNAseq data were compared with publically available RNAseq data for blood Ly6C⁺ and Ly6C⁻ monocytes (Mildner et al., 2017). Each column represents consolidated data from at least three biological replicates per cell type. The z-score of the gene expression profiles gives a scale to measure the differential expression. **(B)** PCA of the transcriptional signature obtained by RNAseq data comparing eWAT monocytes to blood Ly6C⁺ and Ly6C⁻ monocytes depicted in A. **(C and D)** Volcano plots depicting genes differentially expressed by eWAT monocytes in relation to blood Ly6C⁺ (C) and Ly6C⁻ (D) monocytes. Genes differentially expressed with high expression difference and/or high adjusted P values are labeled in red. Consolidated data from at least three biological replicates. **(E)** Heat map displaying selected genes that are differentially expressed between eWAT monocytes and Ly6C⁺ and Ly6C⁻ blood monocytes. Consolidated data from at least three biological replicates. **(F)** Turnover kinetics of Ly6C⁺ monocytes. WT animals were injected once i.p. with 1 mg of BrdU, and the decay of BrdU⁺ labeling was analyzed 12, 24, 48, 72, and 96 h after the BrdU injection in the indicated organs (*n* = 3 per group, representative of two independent experiments). **(G)** Fate mapping of monocytes and VAM populations. Tamoxifen was administered to *Cx3cr1*$^{\text{Cre-ERT2-YFP}}$ × *Rosa26*$^{\text{LSL-DsRed}}$ mice twice 24 h apart by gavage, before starting the time course. Animals were analyzed 1, 5, 10, 20, and 40 d after the last injection of tamoxifen. Microglia are shown as a well-established internal positive control for DsRed labeling (Parkhurst et al., 2013; *n* = 3 per group, representative of two independent experiments). **(H)** Most myeloid eWAT subpopulations are derived from blood progenitors. CD45 congenic animals were precisely irradiated in the hind limbs using an X-RAD 320 (PXI) irradiator, preserving the rest of their bodies from irradiation. Congenic bone marrow (BM) was transferred i.v., and 8 wk later cell chimerism was assessed in the adipose tissue (indicated as percentage of CD45.2 cells among the total population); *n* = 4 per group, representative of two independent experiments. Graphs are shown as mean ± SEM.

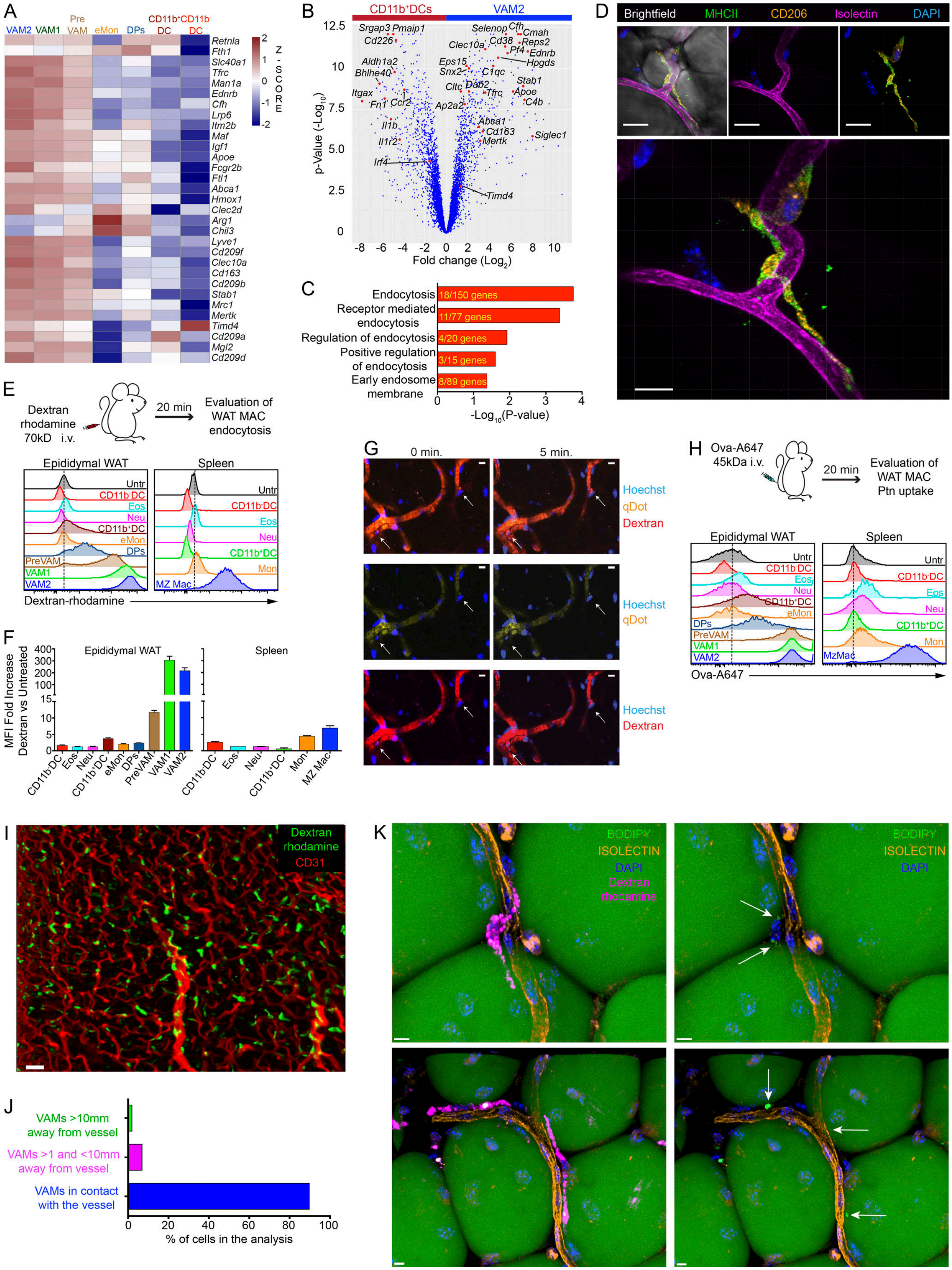
A
VAM2
VAM1
Pre VAM
eMon
DPs
CD11b+ DC
CD11b- DC
Retnla
Fth1
Slc40a1
Tfrc
Man1a
Ednrb
Cfh
Lrp6
Itm2b
Maf
Igf1
Apoe
Fcgr2b
Ftl1
Abca1
Hmox1
Clec2d
Arg1
Chil3
Lyve1
Cd209f
Clec10a
Cd163
Cd209b
Stab1
Mrc1
Mertk
Timd4
Cd209a
Mgl2
Cd209d
Z-SCORE
2
1
0
-1
-2
B
CD11b+DCs
VAM2
p-Value (-Log10)
Fold change (Log2)
Srgap3
Pmaip1
Cd226
Aldh1a2
Bhlhe40
Itgax
Fn1
Ccr2
Il1b
Il1r2
Irf4
Selenop
Cfh
Cmah
Clec10a
Cd38
Reps2
Pf4
Ednrb
Hpgds
Eps15
Snx2
C1qc
Stab1
Cltc
Dab2
Tfrc
Apoe
Ap2a2
C4b
Abca1
Cd163
Mertk
Siglec1
Timd4
C
Endocytosis
Receptor mediated endocytosis
Regulation of endocytosis
Positive regulation of endocytosis
Early endosome membrane
18/150 genes
11/77 genes
4/20 genes
3/15 genes
8/89 genes
-Log10(P-value)
D
Brightfield
MHCII
CD206
Isolectin
DAPI
E
Dextran rhodamine 70kD i.v.
20 min
Evaluation of WAT MAC endocytosis
Epididymal WAT
Spleen
Untr
CD11b-DC
Eos
Neu
CD11b+DC
eMon
DPs
PreVAM
VAM1
VAM2
Mon
MZ Mac
Dextran-rhodamine
F
MFI Fold Increase Dextran vs Untreated
Epididymal WAT
Spleen
CD11b-DC
Eos
Neu
CD11b+DC
eMon
DPs
PreVAM
VAM1
VAM2
Mon
MZ Mac
G
0 min.
5 min.
Hoechst
qDot
Dextran
H
Ova-A647 45kDa i.v.
20 min
Evaluation of WAT MAC Ptn uptake
Epididymal WAT
Spleen
MzMac
Ova-A647
I
Dextran rhodamine
CD31
J
VAMs >10mm away from vessel
VAMs >1 and <10mm away from vessel
VAMs in contact with the vessel
% of cells in the analysis
K
BODIPY
ISOLECTIN
DAPI
Dextran rhodamine

Figure 3. **VAMs rapidly and efficiently uptake blood macromolecules. (A)** Heat map of genes differentially expressed in VAMs displaying anti-inflammatory, insulin-sensitizing, repair, and detoxifying gene signatures. Each column represents consolidated data from three biological replicates. The z-score of the gene expression profiles gives a scale to measure the differential expression. Adult (average 16-wk-old, range 12–20) WT males were used. **(B)** Volcano plot comparing the top 7,000 genes expressed by VAM2 and CD11b$^+$ DCs from eWAT. Signature genes are labeled in red. Consolidated data from at least three biological replicates. **(C)** VAM gene signature, analyzed by functional enrichment, reveals an association with endocytic activity. Consolidated data from at least three biological replicates. **(D)** VAMs are intimately associated with eWAT vessels. Representative confocal images of epididymal full-mount sections showing the distribution of VAMs (CD206$^+$MHCII$^+$DAPI$^+$) in close contact to vessels labeled with isolectin. Bars, 10 µm. 60× magnification. For contextualization, the three upper panels display the following: VAM among adipocytes, which are shown translucently by the bright field channel (left); blood vessel labeled with isolectin (center); VAM labeled as CD206$^+$MHCII$^+$DAPI$^+$ (right); *n* = 3, representative of five independent experiments. **(E)** VAMs are highly endocytic in vivo. Dextran-rhodamine 70 kD was injected i.v. 20 min after the injection, animals were anesthetized and perfused intracardially. Endocytic activity was evaluated by flow cytometry, which measured rhodamine fluorescence. Histograms display the fluorescence intensity for rhodamine of eWAT and splenic populations. Untr, untreated. CD11b$^-$DC (CD90$^-$CD19$^-$CD11b$^-$MHCII$^+$CD11c$^+$) Eos, eosinophils (CD90$^-$CD19$^-$CD11b$^+$SiglecF$^+$); Neu, neutrophils (CD90$^-$CD19$^-$CD11b$^+$Ly6G$^+$); CD11b$^+$DC (CD90$^-$CD19$^-$CD11b$^+$MHCII$^+$CD11c$^+$) Mon, monocytes (CD90$^-$CD19$^-$CD11b$^+$SiglecF$^-$Ly6G$^-$MHCII$^-$Ly6C^{HIGH}); MZ Mac, marginal zone macrophages (CD90$^-$CD19$^-$CD11b^{INT}CD64$^+$CD206$^+$MHCII$^+$). Representative histogram; *n* = 4, representative of three independent experiments. **(F)** Fold increase of the median rhodamine fluorescence intensity after injection, normalized to the individual autofluorescence of each subpopulation (*n* = 4, representative of three independent experiments). **(G)** Intravital microscopy analysis of eWAT dextran-rhodamine uptake 5 min after i.v. injection (Video 1). qDots (Qtracker 655) and Hoechst were i.v. injected immediately before the beginning of the recording, while dextran-rhodamine was injected while the recording was taking place. 25× magnification. Bars, 10 µm. Representative image; *n* = 3, representative of two independent experiments. The arrows indicates a small field in which VAMs are uptaking dextran-rhodamine. **(H)** VAMs high endocytic capacity in vivo extends to proteins. Whole ovalbumin-A647 (Ova) was injected i.v., and 20 min after injection, animals were analyzed as described in the legend of B. Ptn, protein; MAC, macrophage. Adult (12–16-wk-old) WT males were used. Representative histogram; *n* = 3, representative of two independent experiments. **(I)** Light sheet microscopy of full epididymal fat pad after WAT clarification using Adipo-Clear technique (Chi et al., 2018; Video 2). CD31 marks blood vessels. Animals were injected with dextran-rhodamine and, after 1 h, submitted to sample preparation for Adipo-Clear. Panel shows VAMs around blood vessels from different z stacks. Bar, 50 µm. 4× magnification. Representative image; *n* = 3, representative of three independent experiments. **(J)** Analysis of VAM association with blood vessels was performed using Imaris/Bitplane software. Bar graph represent aggregated results of 2,234 macrophages analyzed distributed over 300 stacks of images acquired in I. **(K)** Representative confocal images of epididymal full-mount sections showing the distribution of VAMs (dextran-rhodamine$^+$DAPI$^+$) in close contact to blood vessels labeled with Isolectin. Bodipy labels lipid droplets, in macrophages and adipocytes. Bars, 5 µm. 63× magnification. Microscopy performed in a high-resolution Zeiss LSM 880 with Airyscan. Lipid droplets inside VAMs are indicated by arrows (Video 3). Representative image; *n* = 3, representative of two independent experiments. Bar graphs are shown as mean ± SEM.

In summary, the gene expression profile, the location in close proximity with the vasculature, and the high endocytic capacity suggest that VAMs contribute to establish and maintain a healthy adipose tissue environment.

Markedly reduced endocytic capacity of eWAT macrophages from mice chronically fed HFD

Having established key properties of eWAT macrophages in mice fed ND, we next assessed the response of the myeloid populations to metabolic and inflammatory stress. First, we studied the myeloid cell populations in mice switched to an HFD (60% of calories from fat, 20% carbohydrates, and 20% protein) for 20 wk (Fig. 4 A). This treatment causes obesity and insulin resistance (Surwit et al., 1988; Rebuffé-Scrive et al., 1993). As expected, HFD induced dramatic changes in the eWAT macrophage populations (Fig. 4, B and C), as well as increases in the eWAT pad size (Fig. 4 D) and the cellularity of the stromal vascular fraction (SVF) and of total CD45$^+$ cells (Fig. 4 E). Confirming what has long been established (Weisberg et al., 2003; Xu et al., 2003), the total number of macrophages per gram of fat was increased (Fig. 4 C). The most apparent change in myeloid cells was the dramatic surge of DP macrophages, which, as mentioned above, express high levels of CD11b, CD11c, CD64, and MHCII and intermediate levels of CD206 (Fig. 4, B and C; Nguyen et al., 2007; Shaul et al., 2010; Wentworth et al., 2010; Zeyda et al., 2010). A recent publication refers to these as CD9 macrophages (Hill et al., 2018), but we prefer to maintain the traditional CD11c-based DP nomenclature, as CD9 expression is proportionally more up-regulated than CD11c expression in VAMs by HFD.

DPs are newcomer macrophages promptly generated from blood monocytes in HFD-fed mice (Fig. 4 F). VAM1 and VAM2 also increased in number during HFD feeding (Fig. 4 C), although they were inefficiently generated by blood monocytes (Fig. 4 F), an observation consistent with the fact that VAMs are tissue resident and are maintained, to a large extent, by self-renewal (Amano et al., 2014). PreVAMs are generated from blood monocytes, although with lower efficiency than DP macrophages, but much higher efficiency than either VAM1 or VAM2 (Fig. 4 F). We performed RNAseq studies of eWAT macrophages from mice fed HFD, including DPs, PreVAMs, VAM1, and VAM2. While the characteristic VAM markers from ND-fed mice were maintained in HFD-fed mice, there was a convergence of the VAM and DP gene expression patterns (Fig. 4 G).

Our transcriptional analysis did not confirm the view that ATMs arising in HFD-fed mice are overtly proinflammatory. DP macrophages arising during HFD expressed high levels of genes encoding potent secreted anti-inflammatory molecules such as IL-10 (*Il10*), TGF-β1 (*Tgfb1*), and IL-1 receptor antagonist (*Il1rn*; Fig. 4, H and I). There was no expression of α, β, or γ interferons and minimal expression of IFN-κ and IL-6 in DP macrophages on VAMs before or during HFD feeding. However, *Tnf*, *Cxcl1*, pro-IL-1β, and *Cd44* were moderately up-regulated. Many of the HFD-induced highly up-regulated genes in eWAT macrophages have been previously ascribed an inflammatory signal-deactivating (*Tnfaip3, Rgs1*) function, an insulin-sensitizing (*Pparg*) function, or detoxifying (*Igf2r, Gpx1, Prdx1, Lrp1*) functions (Fig. 4, H and I). Some of these genes, such as *Lgals3* and *Fabp4*, have been attributed with both pro- or antidiabetogenic functions, depending on the experimental conditions. A number

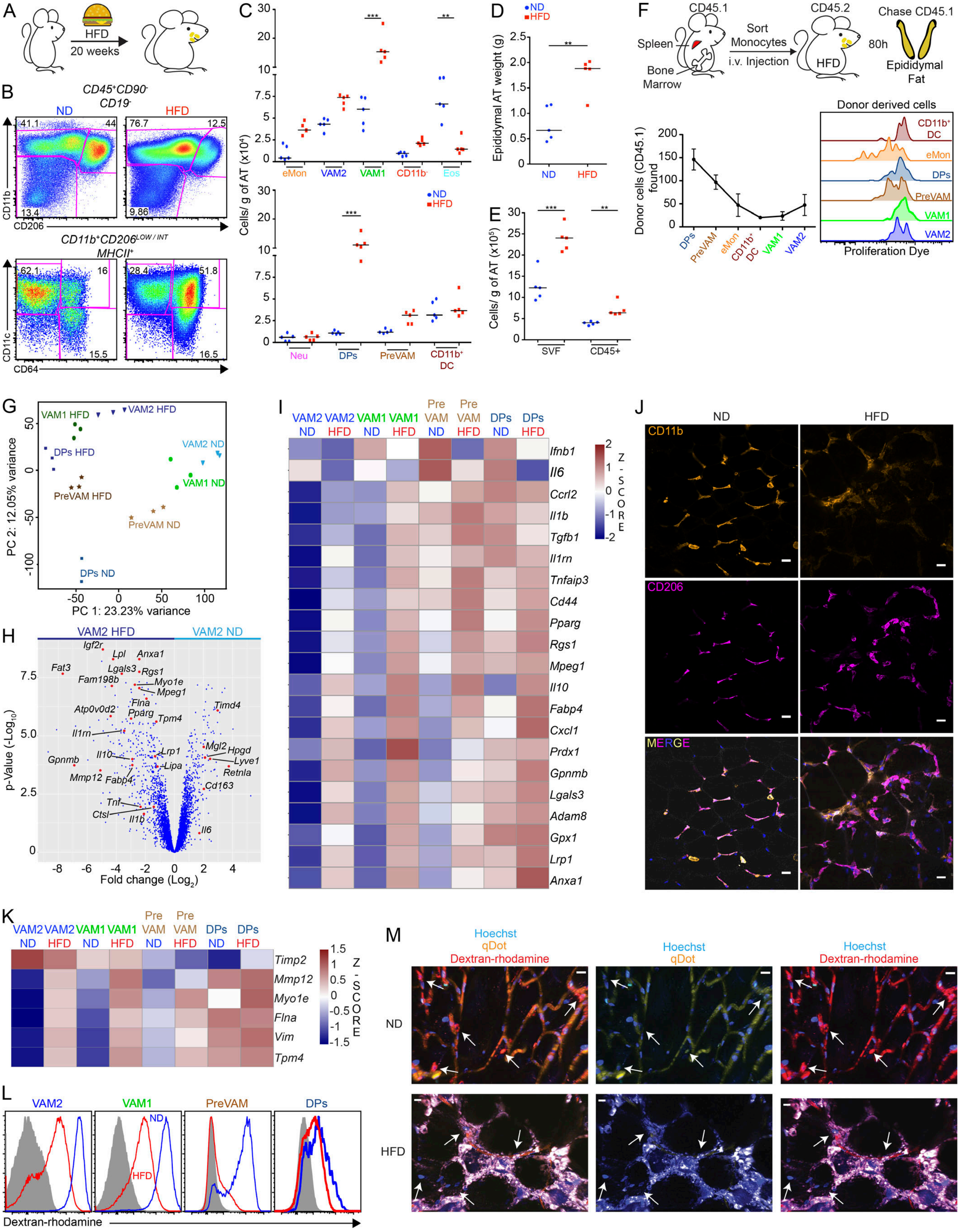
A
HFD
20 weeks
B
CD45+CD90- CD19-
ND
HFD
41.1
44
13.4
76.7
12.5
9.86
CD11b
CD206
CD11b+CD206LOW / INT MHCII+
62.1
16
15.5
28.4
51.8
16.5
CD11c
CD64
C
Cells/ g of AT (x10⁴)
eMon
VAM2
VAM1
CD11b-
Eos
Neu
DPs
PreVAM
CD11b+ DC
ND
HFD
***
**
D
Epididymal AT weight (g)
E
Cells/ g of AT (x10⁵)
SVF
CD45+
F
CD45.1
Spleen
Bone Marrow
Sort Monocytes
i.v. Injection
CD45.2
HFD
Chase CD45.1
80h
Epididymal Fat
Donor cells (CD45.1) found
DPs
PreVAM
eMon
CD11b+ DC
VAM1
VAM2
Donor derived cells
CD11b+ DC
eMon
DPs
PreVAM
VAM1
VAM2
Proliferation Dye
G
VAM1 HFD
VAM2 HFD
DPs HFD
PreVAM HFD
VAM2 ND
VAM1 ND
PreVAM ND
DPs ND
PC 1: 23.23% variance
PC 2: 12.05% variance
H
VAM2 HFD
VAM2 ND
Igf2r
Lpl
Anxa1
Fat3
Lgals3
Rgs1
Fam198b
Myo1e
Mpeg1
Timd4
Atp0v0d2
Flna
Pparg
Tpm4
Il1rn
Mgl2
Hpgd
Lyve1
Il10
Lrp1
Gpnmb
Lipa
Retnla
Mmp12
Fabp4
Cd163
Tnf
Ctsl
Il1b
Il6
p-Value (-Log10)
Fold change (Log2)
I
VAM2 ND
VAM2 HFD
VAM1 ND
VAM1 HFD
Pre VAM ND
Pre VAM HFD
DPs ND
DPs HFD
Ifnb1
Il6
Ccrl2
Il1b
Tgfb1
Il1rn
Tnfaip3
Cd44
Pparg
Rgs1
Mpeg1
Il10
Fabp4
Cxcl1
Prdx1
Gpnmb
Lgals3
Adam8
Gpx1
Lrp1
Anxa1
Z-SCORE
J
ND
HFD
CD11b
CD206
MERGE
K
VAM2 ND
VAM2 HFD
VAM1 ND
VAM1 HFD
Pre VAM ND
Pre VAM HFD
DPs ND
DPs HFD
Timp2
Mmp12
Myo1e
Flna
Vim
Tpm4
Z-SCORE
L
VAM2
VAM1
PreVAM
DPs
ND
HFD
Dextran-rhodamine
M
Hoechst
qDot
Dextran-rhodamine
ND
HFD

Figure 4. **DIO promotes a gene signature enriched in anti-inflammatory genes in eWAT macrophages. (A–C)** WT C57BL/6J male mice (4–6-wk-old) were placed on the HFD OpenSource D12492i for 20 wk or kept on ND. **(B)** Flow cytometry analysis of eWAT macrophage distribution. Representative dot plot; *n* = 3–5 per group, representative of three independent experiments. **(C)** Myeloid cell distribution of WAT macrophages per gram of adipose tissue. **(D)** Epididymal adipose tissue weight. **(E)** eWAT SVF and eWAT CD45$^+$ cell distribution of ND and HFD-fed animals. Data representative of three independent experiments (*n* = 3–5 per group). **(F)** DP macrophages can be generated from monocytes. Ly6C^{HIGH} monocytes from bone marrow and spleen from CD45.1 WT lean mice were labeled with the Cell Proliferation Dye eFluor 450 and injected i.v. into CD45.2 HFD-fed WT mice. 80 h after injection, the transferred cells were quantified and characterized by flow cytometry. Representative data of two independent experiments (*n* = 3 each experiment). Data shown as mean ± SEM. **(G)** PCA of the transcriptional signature obtained by RNAseq data from the populations VAM2, VAM1, PreVAM, and DPs of ND- and HFD-fed animals. Each dot represents data from one animal's epididymal fat pads. **(H)** Volcano plot comparing the top 7,000 genes expressed by VAM2 of ND- and HFD-fed animals. Very similar genes arise when the comparison is made with DP macrophages from HFD-fed mice (data not shown). Consolidated data from at least three biological replicates. **(I)** Heat maps of genes differentially expressed by eWAT macrophages in HFD-fed mice. Each column represents consolidated data from three biological replicates per cell type. The z-score of the gene expression profiles gives a scale to measure the differential expression. Each column represents consolidated data from three biological replicates. **(J)** Representative confocal images of epididymal adipose tissue full-mounted sections of lean (ND) and obese (HFD) male mice showing the distribution of CD206$^+$CD11b$^+$ (VAM) macrophages contouring adipocytes. Bars, 10 µm. 25× magnification; *n* = 3, representative of two independent experiments. **(K)** Heat maps of genes encoding cytoskeletal proteins. Each column represents consolidated data from three biological replicates per cell type. The z-score of the gene expression profiles gives a scale to measure the differential expression. Each column represents consolidated data from three biological replicates. **(L)** VAM endocytic activity in vivo after chronic HFD feeding. Dextran-rhodamine 70 kD was injected i.v., and 20 min after injection, animals were anesthetized and perfused intracardially. The endocytic activity of the indicated eWAT populations was quantified by the fluorescence intensity of rhodamine, as determined by flow cytometry. Representative histogram; *n* = 4, representative of two independent experiments. **(M)** Intravital microscopy analysis of eWAT dextran-rhodamine uptake in mice fed ND or HFD (Video 4). qDots (Qtracker 655), Hoechst, and dextran-rhodamine were i.v. injected, and uptake of rhodamine was observed for 30 min. 25× magnification. Bars, 20 µm. Arrows in the ND-fed samples indicate VAMs uptaking rhodamine. Arrows in the HFD samples point to nucleated cells in tight proximity with blood vessels, which did not uptake rhodamine. Red labeling traces the blood vasculature. Representative image; *n* = 3, representative of two independent experiments. **, $P \leq 0.01$; ***, $P \leq 0.001$. Statistical analysis was performed using unpaired *t* test. AT, adipose tissue.

of beneficial genes highly up-regulated by HFD in eWAT macrophages are involved in lysosomal functions, as previously reported (Xu et al., 2013), or in facilitating digestion of excess lipids (Singh and Cuervo, 2012; Aouadi et al., 2014; Fig. 4, H and I).

In conclusion, the gene expression pattern showed that both the newcomer CD11c$^+$CD64$^+$CD206^{INT} DP macrophages, as well as the preexisting (and also expanded) CD206^{HIGH} VAMs, appear more involved in suppressing the negative consequences of HFD treatment than in the promotion or propagation of these negative effects.

The elongated shape of VAMs observed in mice fed ND was noticeably altered by HFD, with a predominance of rounded CD206$^+$ macrophages in mice fed HFD (Fig. 4 J). Adipocytes were larger, and macrophages acquired a rounder morphology. As previously noticed (Cinti et al., 2005), the number of crown-like structures greatly increased under HFD. These morphological changes may have a correlate in the gene expression profile. Among the genes up-regulated by eWAT macrophages in mice fed HFD were several that affect the cytoskeleton of macrophages, such as *Myo1E*, *Tpm4*, *Flna*, and *Vim*, or alter the extracellular matrix, such as *Mmp12* and *Timp2* (Fig. 4 K). We sought to determine whether these morphological and genetic changes had functional consequences. Mice were injected with dextran-rhodamine i.v. and, after 20 min, were sacrificed to analyze rhodamine uptake. Indeed, there was a significant reduction in the uptake of rhodamine by eWAT macrophages from HFD-fed mice, compared with ND-fed mice (Fig. 4 L). To visualize the uptake in vivo, we performed intravital microscopy, which confirmed the impaired uptake of the dye, and allowed us to visualize crown-like structures in live mice (Video 4 and Fig. 4 M). In summary, our data show that the remarkable endocytic activity displayed by VAMs from ND-fed mice is highly impaired in HFD-fed mice, which could potentially affect their protective function.

Fasting reduces the number of VAMs

Given the remarkable redistribution of VAMs and DP macrophages upon overnutrition, we assessed the impact of acute nutritional restriction (24-h fasting) on eWAT macrophages (Fig. 5 A). Upon food withdrawal, blood glucose levels decrease and lipolysis is triggered, which results in the release of nonesterified fatty acids (FFAs) into the serum. To test some metabolic parameters in mice under our conditions, we quantified serum FFAs, blood glucose, and weight loss during a 24-h fasting experiment. Serum FFA concentration peaked at ∼12–16 h of fasting, indicating a net lipolysis and release of FFAs, and thereafter serum FFA concentrations reached a plateau or diminished slightly (Fig. S3, A and B). As expected, blood glucose decreased early (Fig. S3 C). After 24 h of fasting, body weight loss was ∼10% (Fig. S3 D). Myeloid cells were dramatically reduced by 1-d fasting, with VAMs being the most affected (Fig. 5, A, B, and E). Not only VAMs were reduced; also PreVAMs, eosinophils, and both CD11b$^+$ and CD11b$^-$ DCs were reduced (Fig. 5 B). Unlike HFD, fasting did not provoke an increase in the DP macrophage population; instead, it dropped, albeit nonsignificantly. An overview of the CD45$^+$ eWAT cell landscape upon nutritional restriction can be observed in Fig. 5 E. Interestingly, VAM decrease was almost completed after only 6 h of food deprivation (Fig. S3 E). The cells that were no longer in the eWAT could not be detected either in the spleen or in draining LNs (Fig. S3 F). To assess apoptosis, we determined the expression of active caspase-3, the main executioner of caspase during apoptosis, by flow cytometry. We did not detect a surge in active caspase-3 concomitantly with the rapid cell decrease (Fig. S3, G and H). In fact, active caspase-3 labeling of VAMs is always low, compared with other eWAT cell types. After 24 h of

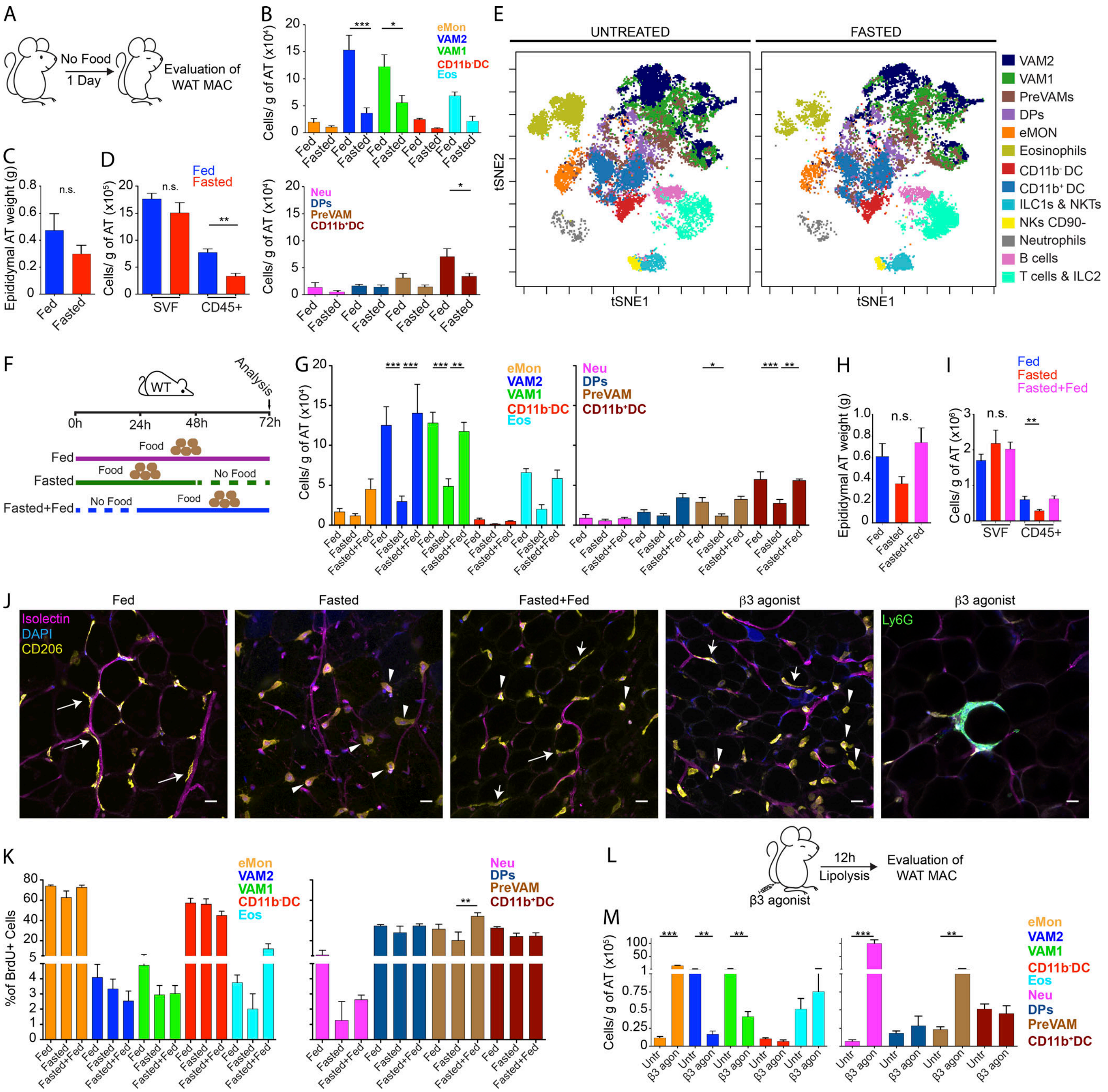

Figure 5. **Fasting swiftly reduces the number of eWAT VAMs. (A–D)** WT mice were fasted for 1 d, and the distribution of eWAT myeloid cells was evaluated by flow cytometry. **(A)** Experimental scheme. **(B)** Myeloid cell distribution of eWAT macrophages per gram of adipose tissue. **(C)** Weight of the epididymal adipose tissue. **(D)** Absolute numbers of cells from SVF and CD45⁺ cells in animals fed and fasted for 24 h. Representative data of three independent experiments (*n* = 3–5 mice per group). **(E)** t-SNE map displaying the eWAT CD45⁺ cell landscape from WT mice fed or fasted and analyzed by flow cytometry. Colors correspond to Cytobank-guided clustering of cell populations. Representative data of three independent experiments (*n* = 3–5 mice per group). **(F–I)** Recovery of eWAT VAM numbers after food was given back. WT mice were fasted for 1 d (fasted), fasted for 1 d followed by recovery in ND for 2 d (fasted+fed), or never deprived of food (fed), as schematically shown in F. **(G)** Myeloid cell population numbers in the eWAT. **(H)** Epididymal adipose tissue weight. **(I)** Absolute numbers of cells from SVF and CD45⁺ cells. Representative data of two independent experiments (*n* = 3–5 mice per group). **(J)** Representative confocal images of epididymal full-mount sections of WT mice fed, fasted, fasted+fed, or treated with the β3 adrenergic receptor agonist CL 316,243. Pictures show the distribution and morphology of VAMs alongside vasculature (labeled with Isolectin) and contouring adipocytes. Arrows, elongated CD206⁺DAPI⁺ VAMs in steady state; arrowheads, rounded CD206⁺DAPI⁺ VAMs in fasted or β3 agonist (CL 316,243)-treated mice. The far right panel shows an atypical crown-like structure formed by accumulation of neutrophils (Ly6G⁺) around an adipocyte. Bars, 10 µm. 25× magnification; *n* = 3, representative of three independent experiments. **(K)** Proliferation of the different myeloid cell populations shown in F–I, as determined by BrdU incorporation. 1 mg of BrdU was injected four times i.p. 12 h apart in the last 48 h of the experiment. Representative data from two independent experiments (*n* = 3–5 per group). **(L and M)** Lipolysis was induced in WT mice by i.v. injection of β3 adrenergic receptor agonist CL 316,243, without food withdrawal. 12 h after injection, the distribution of myeloid cells was assessed as indicated above. MAC, macrophages. Representative data from four independent experiments (*n* = 3–5 per group). *, $P \leq 0.05$; **, $P \leq 0.01$; ***, $P \leq 0.001$. Statistical analysis was performed using one-way ANOVA together with Tukey post hoc test or unpaired *t* test (only for pair comparisons). Animals were 12–14 wk old. Bar graphs are shown as mean ± SEM.

fasting, the weight reduction of the eWAT pads was not significantly different (Fig. 5 C), and neither was the number of SVF cells, while the total CD45$^+$ cells were significantly reduced (Fig. 5 D), consistently with the decrease in all major eWAT myeloid cell populations.

In nature, mice must endure fluctuations in the food supply. Given the conspicuous reduction of VAMs that we observed after 1 d of fasting, we surmised that the number of VAMs would rebound in rapid fashion. We therefore placed a group of 1-d fasted animals back on ND and evaluated the myeloid eWAT populations after 2 d back on ND ("fasted+fed"; Fig. 5 F). To have the appropriate controls in the same experiment, we had a group of mice that were normally fed, never fasted ("fed") and a group of mice that were fasted the last day ("fasted"; Fig. 5 F). As expected, animals feeding after fasting quickly reestablished their initial weight (Fig. S3 D). Remarkably, after 48 h of refeeding, the eWAT populations were back to the normal situation (Fig. 5 G). In these "fasting and feeding" experiments, we also did not observe significant changes in the weight of the fat pads (Fig. 5 H) or in the number of SVF cells; however, the reduction and subsequent rebound of the total number of CD45$^+$ cells were statistically significant (Fig. 5 I).

To evaluate the VAM morphology after fasting, we also performed a confocal microscopy analysis. Confocal images of the eWAT showed that, compared with mice fed all along, VAMs (CD206^{HIGH}) from 1-d fasted mice were abnormally rounded in shape, suggesting that they partially lost their contacts with vasculature and adipocytes (Fig. 5 J, second panel from left). We chose a microscope field that contained many VAMs to allow the morphological characterization, while leaving quantitation for the flow cytometry method. The contorted vasculature, which surrounds adipocytes, allowed us to infer the expected reduction in adipocyte diameter upon fasting. VAMs from fasted+fed mice were abundant in number but had only incompletely regained their normal topology (Fig. 5 J, middle panel). Thus, the VAM depletion induced by 1-d fasting is brief and, it appears, fully reversible.

To assess whether the reconstitution of eWAT VAM numbers was due to self-division, we monitored the incorporation of BrdU over the last 48 h of the fasting and refeeding experiment described above. This gave us a fed (baseline) group, a 24-h fasted group, and a group that was fasted and had fed over the last 48 h. BrdU was poorly incorporated by VAMs in all groups evaluated (Fig. 5 K). Most likely, VAMs were generated by monocytes or PreVAMs that had divided before the BrdU pulse and were differentiating to VAMs while the BrdU pulse was ongoing. It thus appears that, to rapidly reconstitute VAMs after fasting, mice made use of monocytes or monocyte-derived PreVAMs.

Fasting causes a series of metabolic changes, of which increased lipolysis is one. It was possible that the VAM reduction was directly caused by lipolysis, with remodeling of the niche that VAMs occupy in steady state, or in response to other metabolic parameters, such as lowering of glucose or insulin. To induce lipolysis without food withdrawal, we administered a β3 adrenergic agonist, CL 316,243 (Yoshida et al., 1994). Adipocytes express β3 adrenergic receptors, which are locally triggered by sympathetic nerve activation, or systemically by adrenal catecholamines (Bartness et al., 2014). Like fasting, CL 316,243 also induced a dramatic drop in VAM populations after 12 h of a single 2-mg/kg dose (Fig. 5, L and M). Intriguingly, there was a major influx of monocytes and neutrophils into the eWAT (Fig. 5 M and Fig. S3, I–L). By confocal microscopy, we could clearly observe that CL 316,243 reduced and changed the morphology of CD206^{HIGH} (VAM) macrophages, and also induced atypical crown-like structures that are composed of Ly6G$^+$ neutrophils, not macrophages (Fig. 5 J, rightmost panel). In sum, both fasting and a β3 adrenergic agonist caused the rapid depletion of VAMs in the eWAT, suggesting that lipolysis itself, and not the nutritional state, is the driving force in the VAM reduction.

We conclude that VAMs from fasted mice are highly sensitive to the nutritional status of the animals. Acute fasting results in an abrupt but transient decrease in VAMs, whereas chronic overnutrition results in VAMs that are partially dysfunctional.

Acute inflammatory stress provokes rapid and reversible changes in eWAT macrophage populations

Having studied the response of eWAT myeloid cells during two models of nutritional stress, we next studied the impact of acute inflammation on the composition of the different myeloid eWAT cell populations (Fig. 6 A). 24 h after i.v. administration of 50 µg LPS, a sublethal dose, the macrophage populations were dramatically changed in frequency and absolute numbers (Fig. 6 B). VAM1 and 2 were rapidly reduced by approximately fourfold, and the number of DP macrophages (CD64$^+$CD11c$^+$) more than tripled (Fig. 6, C and D). These changes were already significant at 12 h (Fig. 6 D). The number of CD11b$^-$ DCs did not change upon acute LPS-driven inflammation, but the number of CD11b$^+$ DCs was greatly reduced within 12 h (Fig. 6 D). Monocytes and neutrophils were increased. Almost all myeloid cell populations returned to the steady state composition by day 5 (Fig. 6 D). Despite the changes in myeloid cell populations, neither the weight of the fat pads nor the total number of SVF cells and CD45$^+$ cells were significantly altered during the 5-d experiments (Fig. 6, E and F). The fact that VAMs decreased rapidly, and, at the same time, DP macrophages increased, made us investigate the possibility that LPS could induce the conversion of VAMs into DP macrophages. To investigate this possible conversion, we used a "functional fate mapping" strategy. We took advantage of the very high endocytic capacity of VAMs to label them with dextran-rhodamine and follow the fate of labeled cells. We injected dextran-rhodamine i.v.; 36 h later, injected LPS i.v.; and 24 h after LPS injection, analyzed the eWAT myeloid cells by FACS (Fig. 6, G and H). As expected, VAMs efficiently took up dextran-rhodamine, which remained in the few VAMs found after LPS treatment (Fig. 6 H). Importantly, the DP macrophages were not labeled with rhodamine, indicating that they did not derive from converted VAMs (Fig. 6 H). Most likely, they are derived from circulating monocytes, similarly to the equivalent DP population that robustly expands in the eWAT during HFD feeding. In contrast to VAMs, PreVAMs lost their rhodamine after LPS treatment (Fig. 6 H), suggesting they

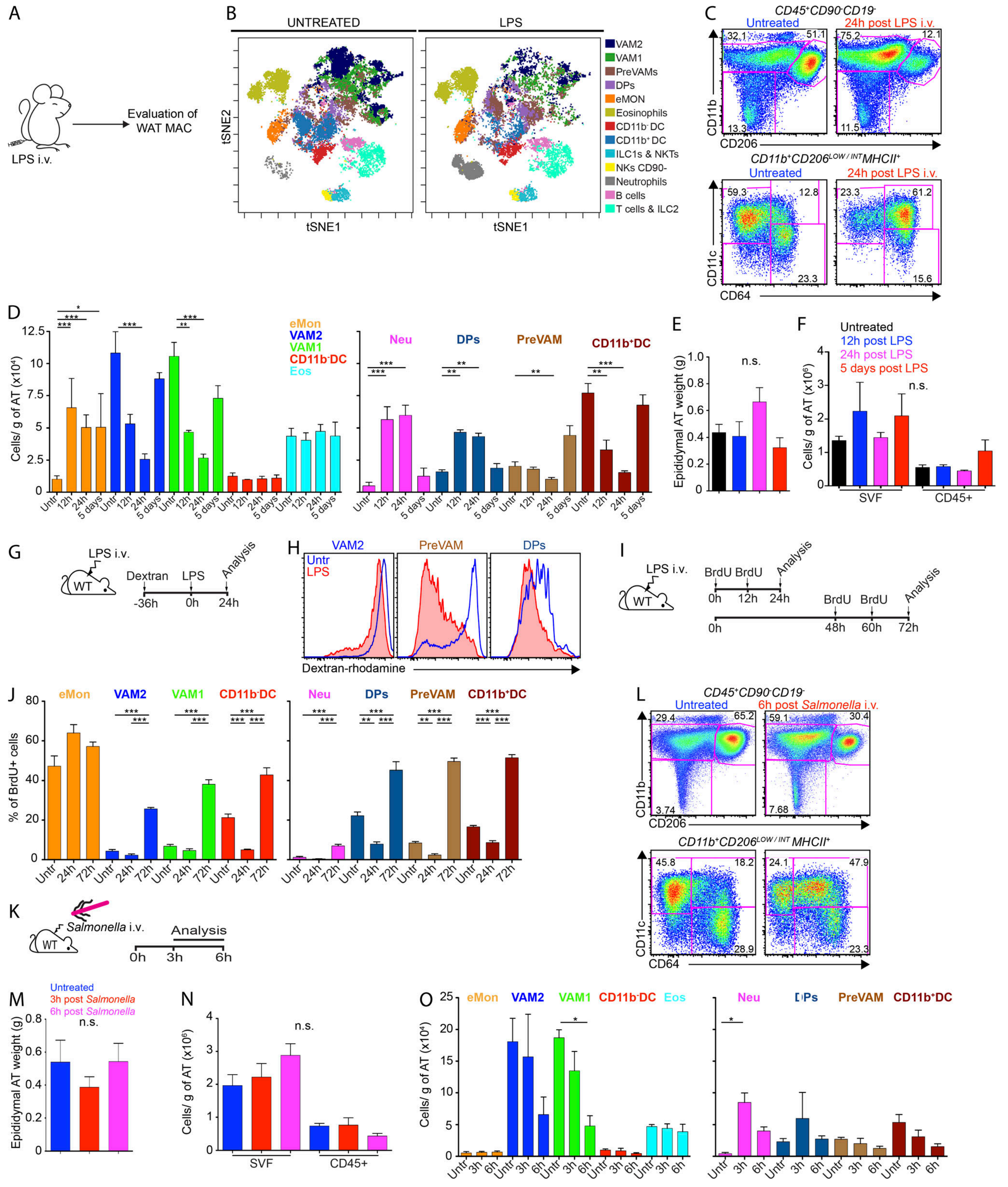

Figure 6. **Differential response of eWAT macrophage subpopulations to systemic acute inflammatory challenges. (A–F)** WT mice were injected with 50 µg of LPS i.v., and the eWAT myeloid cell composition was determined 12, 24, and 120 h after injection. **(B)** t-SNE map displaying the eWAT CD45⁺ cell landscape from untreated or LPS-treated WT mice, analyzed by flow cytometry. Colors correspond to Cytobank-guided clustering of cell populations. **(C)** Flow cytometry. **(D)** Absolute number of eWAT myeloid cells. **(E)** Epididymal adipose tissue weight. **(F)** SVF and total CD45⁺ absolute cell number. Representative data of three independent experiments (*n* = 3–5 mice per experiment). **(G and H)** Functional fate mapping of VAMs exposed in vivo to LPS. WT mice were injected i.v. with dextran-rhodamine 70 kD. 36 h later, the same animals were injected i.v. with 50 µg of LPS. 24 h after the LPS injection, eWAT macrophages were analyzed by flow cytometry. Data representative of two independent experiments (*n* = 3 per group). **(I and J)** eWAT myeloid cell proliferation determined

by BrdU incorporation at different time points. WT animals were injected i.p. twice with 1 mg of BrdU, 12 h apart. BrdU injections started concomitantly with the LPS injection or 48 h after LPS injection. Animals were analyzed at 24- or 72-h time points. Representative data from two independent experiments ($n = 3–5$ per group). **(K–O)** WT mice were inject i.v. with 10^8 CFU of *S. enterica* serovar Typhimurium (*Salmonella*) and eWAT myeloid cell composition was determined 3 and 6 h after infection. **(L)** Flow cytometry. **(M)** Epididymal fat weight. **(N and O)** SVF, total CD45$^+$, and eWAT myeloid cell population, absolute numbers. Representative data of two independent experiments ($n = 3–5$ mice). *, $P \leq 0.05$; **, $P \leq 0.01$; ***, $P \leq 0.001$. Statistical analysis was performed using one way ANOVA together with Tukey post hoc test. AT, adipose tissue. Animals were 12–15 wk old. Bar graphs are shown as mean ± SEM.

were quickly replaced by unlabeled cells, as we know to be the case in mice kept in steady state (Fig. 2 G).

If the rapid reduction in VAM numbers was due to a rare emigration of mature tissue macrophages from eWAT, two of the possible alternative locations would be the spleen, if VAMs emigrate via blood, or the eWAT-draining LNs, if they emigrate via lymph. We therefore determined the myeloid changes in the spleen and draining LNs 24 h after i.v. LPS injection. Macrophages with the surface profile of VAMs were not found in the spleen, while the number of splenic marginal zone macrophages was not significantly changed (Fig. S4 B). We also determined whether VAMs could emigrate to the eWAT draining LNs rapidly upon LPS treatment; however, we detected neither an increase in CD11b$^+$CD206^{HIGH}CD64^{HIGH} cells in the draining LN nor an increase in dextran-rhodamine$^+$ cells, an approach that would have captured emigrating VAMs even if they had suddenly changed their phenotype (Fig. S3 F). We did not observe an increase in active caspase-3 in any eWAT myeloid population (Fig. S4 C). Thus, LPS causes rapid changes in the eWAT myeloid cells, with a reduction in VAMs that we cannot ascribe to differentiation into a different cell type, emigration to the spleen or draining LNs, or caspase-3–mediated apoptosis.

As the number (and proportion) of VAMs is rapidly and dramatically reduced by LPS, it is equally remarkable that the VAM populations return to steady state numbers by 5 d after LPS administration (Fig. 6 D). Given the fact that WAT macrophages have been shown to divide locally (Amano et al., 2014), we speculated that, after LPS, the repopulation of VAMs would take place by their own cell division. We therefore monitored cell division by BrdU incorporation over the first and third days of the experiment (Fig. 6 I). Without LPS, more than half of eWAT monocytes, expectedly, become BrdU$^+$ during the 24-h labeling (Fig. 6 J). VAMs incorporated a very low amount of BrdU. Among macrophages, DPs and PreVAMs, the two populations that we showed to be monocyte-derived, are the only populations with a measurable BrdU incorporation (Fig. 6 J). Upon LPS treatment, BrdU incorporation into VAMs remained very low during the first day, but increased at the third day (Fig. 6 J). This is the time in which the VAMs begin their recovery from LPS. This result is compatible with the self-division of VAMs that was discussed above, but it does not exclude that dividing monocytes took up BrdU and differentiated into VAMs.

To assess whether bacterial infections could also cause a rapid alteration in the composition of the eWAT myeloid compartment, we infected mice with the Gram-negative bacteria, *S. enterica* serovar Typhimurium (hereafter *Salmonella*; Fig. 6 K). *Salmonella* septicemia is a dangerous complication of *Salmonella* infections; therefore, to study this sequela, we injected the bacteria i.v. Similarly to LPS, systemic *Salmonella* infection rapidly caused a reduction of VAMs by 3 and 6 h (Fig. 6, L and O). Also similarly to LPS, *Salmonella* caused an increase in DP macrophages, although it was of shorter duration than the increase caused by LPS, and lower in magnitude (Fig. 6 O). Neither the weight of the fat pads nor the total number of SVF cells and CD45$^+$ cells were significantly altered during the early hours after infection (Fig. 6, M and N).

Thus, the common feature of LPS and a live Gram-negative bacterial infection is that both induce a very rapid reduction in number and frequency of eWAT VAMs, with increase in DP macrophages. Alterations in eWAT myeloid cells were not, however, limited to LPS and Gram-negative bacteria. Infection with the Gram-positive bacteria *Staphylococcus aureus* also resulted in a decrease in the number of VAMs (Fig. S4, F–J), more markedly in VAM1 (Fig. S4 H). Analogous to LPS administration, *S. aureus* infection caused an increase in the proportion of eWAT monocytes (Fig. S4 H).

We conclude that LPS or systemic bacterial infections have an immediate impact on the composition of eWAT myeloid cells, in particular causing a reversible decrease in VAMs. In this regard, both acute infections and fasting affect VAMs in a similar fashion. Our results therefore show a striking adaptation of ATMs to diverse environmental challenges.

Discussion

In this report, we characterized the behavior of the different murine eWAT macrophage populations in the steady state and in response to chronic and acute inflammatory and metabolic stress. By gene expression profiling, flow cytometry, and imaging, we could distinguish four populations of macrophages, which we refer to as VAM1 and VAM2, PreVAM, and CD64$^+$CD11c$^+$ DP macrophages. In steady state, VAM1 and VAM2 are the two dominant myeloid populations by far. Previous characterization of ATMs in steady state mice undoubtedly included these macrophages. Although steady state VAM1 and VAM2 poorly express two of the more typical M2 macrophage genes, arginase 1 (*Arg1*) and chitinase-like 3 (*Chil3*), the overall expression pattern resembles M2 macrophages, as they express high levels of CD206, CD301a, CD163, CD209, and *Retnla*/Fizz1. They express genes that allow the uptake of apoptotic cells, many scavenger receptors, and antioxidant and detoxifying molecules. The most previously underappreciated aspect of the steady state VAMs is their very close contact with vessels, leading to an ultrarapid endocytic capacity of diverse macromolecules present in the bloodstream. This occurs in the absence of any obvious vascular discontinuity. VAMs' high endocytosis, gene expression, and lipid droplets suggest that, in mice fed an ND, VAM1 and VAM2 are not passively waiting for disturbance, but rather, they are active under steady state. VAM properties suggest that a possible function of these tissue-resident macrophages is to keep clean the eWAT adipose tissue environment, both by removing noxious catabolites from the adipocytes and by acting as intermediaries between the blood and the adipocytes. A correlation between phagocytosis capacity, CD206 expression, and tissue homeostasis by macrophages in different organs has recently been reported (A-Gonzalez et al., 2017).

Over the past decade, it has become apparent that many tissue-resident macrophages are not derived from bone marrow progenitors, via circulating monocytes, as had previously been thought (Schulz et al., 2012; Ginhoux and Guilliams, 2016). Typical examples of self-renewing non–bone marrow–derived macrophages in adult animals are microglia and Langerhans cells (Merad et al., 2002; Ajami et al., 2007; Chorro et al., 2009; Ginhoux et al., 2010). In the adipose tissue, self-renewal of macrophages was also shown to be the case (Amano et al., 2014). Indeed, we showed that VAM1 and VAM2 macrophages from steady state mice are not efficiently generated by bone marrow precursors, or by monocytes, although DP macrophages are.

We studied the dynamics of eWAT myeloid cells under three types of nutritional or inflammatory stresses: chronic HFD feeding, fasting, and acute systemic infections. In animals fed HFD, the most striking quantitative change was the increase in the representation of DP macrophages, which are CD11c$^+$ monocyte-derived macrophages whose numbers increased by approximately one order of magnitude. The number of VAM 1 and VAM2 macrophages also increases in response to HFD, but to a lower degree. The most striking qualitative change that we observed in VAMs was their impaired endocytic capacity. The degree by which the impaired endocytic capacity of VAMs contributes to obesity-related disease remains unknown; however, it is possible that the removal of toxic catabolites becomes impaired.

We compared gene expression of all macrophage types in mice chronically fed HFD with that of mice fed ND. In general, whatever gene expression changes were induced by HFD in DP macrophages were also induced in VAMs, although the degree of the changes can be different for DP or VAMs. In fact, we know of no gene whose expression is highly up-regulated in DP macrophages and decreased in VAMs in mice fed HFD, or vice versa. Our gene expression work shows no evidence of an M2 to a classically activated/M1 shift during DIO. Gene expression of VAMs or DP macrophages cannot be defined as M1 or M1-like. Our data are more compatible with the category of "metabolically activated" macrophages (MMe), discovered by stimulating M0 macrophages in vitro with a mixture of insulin, glucose, and palmitate (Kratz et al., 2014), and subsequently validated ex vivo. The MMe activation is independent of proinflammatory signals (Kratz et al., 2014). Among the key MMe genes, *Cd36* and *Plin2* are highly up-regulated in our eWAT samples by HFD, and thus in good agreement with the MMe nomenclature. However, we did not observe up-regulation of *Abca1*, *Acsl1*, *Bag6*, *Dhcr7*, *Far1*, *Plxnb2*, or *Ptprj*. Our gene expression data on macrophages from mice fed HFD also showed activation of lysosomal metabolism and of genes encoding anti-inflammatory molecules such as A20 (*Tnfaip3*), the IL-1 receptor antagonist (*Il1rn*), IL-10, and TGF-β1, in broad agreement with other authors (Xu et al., 2013; Fitzgibbons and Czech, 2016; Coats et al., 2017).

The most striking change induced by acute 1-d fasting in the eWAT myeloid cell populations is their rapid decrease in numbers, which is more marked for VAMs. In the life of wild mice, fluctuations in dietary intake are to be expected. In this context, the rapid and reversible reduction in eWAT VAMs, eosinophils, monocytes, and DCs is remarkable. Fasting-induced lipolysis provides circulating FFAs, which can be used by other cells (e.g., skeletal muscle cells, hepatocytes) to provide energy. During this fasting period, the liver is known to activate gluconeogenesis in response to ghrelin, thus maintaining blood glycemia at acceptable levels. Lipolysis causes, naturally, adipocytes to shrink, and we speculate that this change in size removes cytoskeletal cues from the VAMs, possibly causing a number of them to undergo cell death. Thus, adipose tissue remodeling could induce the loss of VAMs. The effect of fasting on eWAT macrophages was mimicked by a β3 adrenergic agonist, CL 316,243, in conditions of food availability. These results support the view that lipolysis itself, not the nutritional state, caused the loss of VAMs. However, basal lipolysis, such as the one induced by chronic HFD feeding in the presence of hypertrophic adipocytes (Duncan et al., 2007; Zechner et al., 2009), caused an increase in VAMs.

Interestingly, in a model of adipocyte cell death caused by overexpression of an active caspase-8, Fischer-Posovszky et al. (2011) described an increase of macrophages that displayed an M2 activation profile, which we are here referring to as VAMs. Since fasting-induced lipolysis does not involve massive cell death, our results showing VAM reduction are entirely compatible.

The strong inflammatory response to a single CL 316,243 dose was not unexpected, but did not occur with acute fasting within the 24-h time frame that we studied. It was reported that one i.p. treatment with CL 316,243 resulted in an increased myeloid population in the WAT after 6 h (Mottillo et al., 2007). Chronic CL 316,243 treatment with osmotic pumps was reported to cause rapid inflammation in the adipose tissue, which was more marked in PPARγ-deficient than WT mice (Li et al., 2005). Kosteli et al. (2010) administered CL 316,243 i.p. and observed an increase in F4/80 staining by immunohistology after 18 h. Considering that F4/80 is expressed by both eWAT macrophages and monocytes, it is possible that the increase in total F4/80 cells reported by Kosteli et al. (2010) reflects the balance between the increase in monocytes that we observed and the decrease in VAMs that we also observed. It is possible that the discrepancy between the neutrophilia induced by CL 316,243 and not by 1-d fasting lies in the fact that, besides lipolysis, CL 316,243 also induces thermogenesis (Kazak et al., 2017). β3 Adrenergic agonists are currently approved by the US Food and Drug Administration for human use in overactive bladder syndrome (Takasu et al., 2007; Malik et al., 2012) and have been discussed as anti-obesity and insulin-sensitizing treatments for humans (Arch, 2008; Cypess et al., 2015). It is therefore important that the basis of the proinflammatory response caused by β3 adrenergic agonists be further studied.

Intriguingly, upon acute stress caused by i.v. LPS or bacterial infections with *Salmonella* or *S. aureus*, the number and proportion of VAMs decreases substantially and returns to normal shortly after the stressful condition is removed. Since this phenomenon was also observed after acute fasting, this dynamic fluctuation seems to be a common response to acute stress. Bacterial infections (or LPS treatment) cause metabolic changes in the host, which in turn may be associated with rapid changes in adipose myeloid cell composition. Infections induce "sickness behavior," whereby the host reduces food consumption, triggering gluconeogenesis and lipolysis, and a higher brain consumption of ketone bodies (O'Neill and Hardie, 2013; Wang et al., 2016). LPS itself was shown to increase glucose uptake and aerobic glycolysis in macrophages (Krawczyk et al., 2010; Palsson-McDermott et al., 2015). Thus, the rapid and reversible reduction of eWAT VAMs could be part of a global response of the eWAT to acute stress, be it infectious or nutritional.

In contrast to the acute fasting, systemic bacterial infections or LPS triggered an increase in DP macrophages in the eWAT, whereas VAMs were decreased by both types of stress. Although DP macrophages induced by HFD feeding and LPS share the expression of all the key surface markers, we do not presently know the precise degree of similarity between DP macrophages elicited by systemic infections of chronic HFD feeding.

In both nutritional and inflammatory acute stresses, there is a rapid reduction and subsequent recovery of VAM numbers. In the case of LPS-induced VAM reduction, we observed BrdU incorporation in VAMs at the time of their recovery (Fig. 6 J), confirming that they are self-dividing tissue-resident macrophages. However, in the case of fasting, we did not detect BrdU incorporation in VAMs at any time point (Fig. 5 K). In this case, the most likely source of VAMs are PreVAMs, or monocytes. PreVAMs have a gene expression signature that is quite similar to that of VAMs (Fig. 1, D–F; and Fig. 3 A), and they display intermediate endocytic capacity compared with that of VAMs (Fig. 3, E and H). We showed that, unlike VAMs, PreVAMs are generated from bone marrow precursors (presumably via monocytes) in mice fed ND or HFD (Fig. 2, G and H; and Fig. 4 F). Under normal conditions, PreVAMs turn over rapidly, as shown by their basal BrdU incorporation being higher than VAMs (Fig. 5 K); their steady state numbers are one order of magnitude lower than the VAMs (Fig. S1 K). The totality of the data are therefore consistent with a model whereby PreVAMs are continuously being generated from monocytes, but they do not become VAMs unless a major VAM replacement is needed, for example in the recovery from fasting.

We analyzed the rapid reduction of VAMs in more detail. We determined that the VAMs were not converting to other eWAT cell types and that they did not emigrate to the spleen or draining LNs. Although mature tissue-resident macrophages such as VAMs are not expected to be migratory, our data do not rule out that, under acute stress, VAMs temporary emigrate to a reservoir outside of spleen and draining LNs, only to return when conditions stabilize. We did not observe signs of caspase-3–mediated apoptosis in VAMs at different time points. Due to the rapid in vivo uptake and destruction of apoptotic cells, it is sometimes difficult to detect active caspase-3 in vivo. Several caspase-3–independent programmed cell death pathways have been reported in the literature (Lee et al., 2006; O'Sullivan et al., 2007). Both necroptosis and pyroptosis occur in the absence of caspase-3 activation; however, at least in the case of fasting, these two pathways are unlikely, as they are considered proinflammatory deaths, and a brief fasting is accompanied by no signs of eWAT inflammation; instead, most inflammatory cells are decreased. It has been long known that, in vitro, LPS or LPS-containing bacteria can cause apoptosis of macrophages (Bingisser et al., 1996; Hilbi et al., 1997; Xaus et al., 2000), but it is also known that LPS is a powerful activator of macrophages, through TLR4 signaling. It has been shown that Gr-1 ILC could kill ATMs (Boulenouar et al., 2017), and that M2 macrophages, such as VAMs, are more efficient targets. It is therefore possible that Gr-1 ILC are the executioners of VAMs very rapidly after acute infectious or metabolic stress.

A major unresolved issue raised by our work is the possible adaptive value of acutely removing potentially valuable macrophages such as VAMs during inflammatory or nutritional stress. During acute infections, it is likely that the monocyte-derived DP macrophages are better equipped than VAMs to participate in pathogen removal functions. It is less clear what the adaptive value of transiently losing VAMs is during fasting, if any. Experiments to address this question directly, such as injecting VAMs to repopulate the WAT, are technically very difficult. The natural depletion of VAMs is also likely to affect the interactions with other immune cells such as effector and regulatory T cells, which abound in WAT. Thus, our characterization of the several different myeloid cell types could help the clarification of the interactions between lymphoid, myeloid, and nonhematopoietic cells in adipose tissue.

In conclusion, we showed how VAMs, which are located at the intersection between the vasculature and the adipose tissue, display an ultra-fast endocytic activity and are very sensitive to different environmental changes, yet maintain a striking capacity for rapid recovery.

Materials and methods

Mice

Foxp3^{GFP} male mice in C57BL/10.PL background (Weiss et al., 2012) and C57BL/6J (000664) purchased from The Jackson Laboratory were used as WT animals throughout the study. B6 CD45.1 (564) animals were purchased from Charles River. CX3CR1-GFP mice (005582) were purchased from The Jackson Laboratory. *Cx3cr1*$^{CRE\text{-}ERT2\text{-}YFP}$ × *Rosa26*$^{LSL\text{-}DsRed}$ was a kind gift of the Wenbiao Gan and Dan Littman laboratories (New York University [NYU] Langone Medical Center, New York, NY; Parkhurst et al., 2013). HFD-fed male mice were treated with an HFD for ≥16 wk starting at 4–6 wk of age. Mice were fed standard chow providing 17% calories from fat (LabDiet Formulab 5008) or an HFD providing 60% calories from fat (Research Diets; D12492i). Blood glucose was determined with a One Touch Basic glucometer (Lifescan). Mice were sacrificed by CO_2 euthanasia, and serum was collected when necessary. Serum analysis of FFAs content was performed using an FFA assay kit (Abcam; ab65341). As indicated in the text, some mice were treated i.v. with 2 mg/kg of β3 receptor agonist (CL 316,243; Tocris; 1499), 50 µg of LPS (Sigma-Aldrich; L4391), 18 mg/kg of dextran-rhodamine 70 kD (Sigma-Aldrich; R9379), 2 mg/kg of OVA-A647 (Thermo Fisher Scientific; O34784), and 10 mg of tamoxifen (Sigma-Aldrich; T5648). Animals were housed at NYU Medical Center Animal Facility under specific pathogen-free conditions. All procedures were approved by NYU School of Medicine Institutional Animal Care and Use Committee.

Adipose tissue SVF purification

To isolate leukocytes from adipose tissue, mice were anesthetized with a mixture containing 12.5 mg/ml ketamine, 2.5 mg/ml xylazine, and 25 mg/ml acepromazine and intracardially perfused with PBS with 5 mM EDTA. After dissection, the fat tissue was minced and incubated for 35 min at 37°C under gentle agitation (150 rpm) in complete Roswell Park Memorial Institute medium (cRPMI; 10% FBS, 1 mM of sodium pyruvate [Gibco; 11360-070], Glutamax 1× [Gibco; 35050-061], MEM nonessential amino acids [Gibco; 11140-050], Hepes [Gibco; 15630-080], penicillin/streptomycin [Gibco; 15140-122], and RPMI [Gibco; 21870-076] containing 1 mg/ml of collagenase type VIII [Sigma-Aldrich; C2139], and 100 µg/ml of DNase I [Sigma-Aldrich; 10104159001]). After digestion, the suspension was washed with ice-cold cRPMI and spun down. The floating fat layer was removed, and the leukocyte-enriched pellet was resuspended in cRPMI and filtered through a 70-µm cell strainer.

Although the RNAseq data shown in this article were obtained following the above extraction method, we also performed a comparative experiment analyzing VAM2, in which we used 2% FFA-free BSA (Thermo Fisher Scientific; BP9704100) in the digestion and staining buffers instead of FBS. RNAseq results between the two extraction methods were highly similar without displaying a single gene with significant adjusted P value. Data are deposited in the Gene Expression Omnibus repository, accession no. GSE126407.

Isolation of mononuclear cells from spleen

Mice were perfused as described above. Spleens were minced and digested in PBS containing 5% FBS, 10 mM Hepes, and 160 U/ml collagenase D (Sigma-Aldrich; 11088882001) at 37°C for 35 min. After incubation, 10 mM EDTA was added for 5 min in to disrupt DC–T cell complexes. The cell suspension was then filtered through a 70-µM cell strainer.

Bacteria

S. enterica serovar Typhimurium (SL1344) strain (Yu et al., 2014) was used in infection experiments. Mice were injected i.v. with 10^8 CFU and analyzed 3–6 h after infection, as indicated. Briefly, a single aliquot of *Salmonella* was grown in 3 ml of LB overnight at 37°C with agitation, and then the bacteria were subcultured (1:30) into 3 ml of LB for 3 h at 37°C with agitation. Bacteria were injected i.v. into recipient mice in a total volume of 100 µl. *S. aureus* strain Newman were cultured overnight from a single colony in 5 ml tryptic soy broth with shaking at 37°C. Cultures were diluted 1:100 in tryptic soy broth (5 ml for i.v. infection) and cultured with shaking at 37°C for an additional 3 h until optical density at 600 nm was 1.5 (10^9 CFU/ml). I.v. infection was performed via retro-orbital vein. Mice were injected i.v. with 10^8 CFU and analyzed 12 h after infection, as indicated.

Antibodies and fluorescent conjugates

The following antibodies were purchased from BD Biosciences: anti-active caspase-3 (clone C92-605) BUV395, 564095; anti-BrdU (clone 3D4) Percp-cy5-5, 560809; anti-CD45 (clone 30-F11) BUV 395, 564279; anti-Ly6G (clone 1A8) Percp-cy5.5, 560602; anti-SiglecF (clone E50-2440) BV421 and APC-R700, 565934 and 565183; and Streptavidin-BUV395, 564176. The following antibodies were purchased from Thermo Fisher: anti-CD8 (clone 53–6.7) APC-E780, 47–0081-82; anti-CD11b (clone M1/70) APC-E780, 47–0112-82; anti-IL33R (clone RMST2-2) PE, 12–9335-82; anti KI-67 (clone SolA15) PE, 12–5698-82; Ovalbumin-A647, O34784; Bodipy 493/503, D3922; Isolectin GS-IB4 A647, I32450; Isolectin GS-IB4 A568, I21412; Qtracker 655 vascular labels, Q21021MP; and Hoechst 33342, 62249. 4′,6-diamidino-2-phenylindole (DAPI), D3571 or live/dead fixable blue, L34961 were used to exclude dead cells. The following were purchased from BioLegend: anti-CD4 Percp-cy5.5 (clone RM4-5), 100540; anti-CD11b (clone M1/70) A488 and A647, 101217 and 101218; anti-CD11c (clone N418) A647, 117312; anti-CD19 (clone 1D3) FITC, 152404; anti-CD31 (clone 390) A647, 102415; anti-CD45 (clone 30-F11) A700, 103128; anti-CD64 (clone x54-5/7.1) APC, PE, BV421 and Biotin, 139306, 139304, 139309 and 139318; anti-CD206 (clone C068C2) A647, PE-CY7 and PE/DAZZLE594, 141711, 141720 and 141731; anti-CD301 (clone LOM-14) Percp-cy5-5, 145709; anti-F4/80 (clone BM8) BV421, 123137; anti-I-A/I-E (clone M5/114.15.2) A488, A647 and BV711, 107616, 107618 and 107643; anti-Ly6C (clone HK1.4) A488 and BV510, 128021 and 128033; anti-Ly6G (clone 1A8) PE/DAZZLE594, 127647; anti-NK1.1 (clone PK136) BV650 and PE/DAZZLE594, 108736 and 108747; anti-γδ TCR (clone GL3) FITC, 118105; anti-Thy1.2 (clone 30-H12) FITC, 105306; anti-TCRβ (clone H57-597) BV510, 109233; and Streptavidin-BV421; 405225. The following was purchased from Sigma-Aldrich: Rhodamine B isothiocyanate-dextran 70 kD; R9379.

Flow cytometry and cell sorting

Flow cytometry data were acquired on an LSR-II flow cytometer (Becton Dickinson) and analyzed using FlowJo software (TreeStar 8.7) and Cytobank (https://www.cytobank.org) for dimensionality reduction and visualization by t-SNE. All stainings were performed as recommended by the antibody manufacturer. All samples were preincubated with Fc block (2.4G2; Bioxcell; BE0307) for 15 min at 4°C. FACS sorting was performed using an ARIA II sorter using a 100-µm nozzle (Becton Dickinson). Flow cytometry of ATMs is made somewhat difficult because of their high autofluorescence. To minimize the impact of autofluorescence, we meticulously selected the fluorochromes for each cell marker and used FMOs.

BrdU incorporation

WT mice were injected i.p. with 1 mg of BrdU as indicated in the figure legends. Spleens and fat pads were harvested and processed as described above. Cells were surface stained and intranuclearly stained for BrdU using the BD BrdU proliferation kit (552598).

Monocyte transfer into HFD-treated animals

To evaluate if ATM subpopulations have origin from circulating monocytes in HFD-treated animals, monocytes were isolated from the spleens and bone marrow of CD45.1 WT mice by flow cytometry sorting as CD45$^+$CD90$^-$CD19$^-$NK1.1$^-$CD11b$^+$LY6G$^-$MHCII$^-$Ly6C^{HIGH}. Sorted cells (2 × 10^6) were injected i.v. into CD45.2 WT mice. After 80 h, adipose tissue cells were isolated and analyzed by flow cytometry.

RNA isolation and sequencing

Total RNA from sorted target cell populations was isolated using TRIzol LS (Invitrogen; 10296010) followed by DNase I (Qiagen; 79254) treatment and cleanup with RNeasy Plus Micro kit (Qiagen; 74034). RNA quality was assessed using Pico Bioanalyser chips (Agilent; 5067-1513). Only RNAs displaying a RNA integrity number of 9 or higher were used for downstream procedures. RNAseq libraries were prepared using the Nugen Ovation Trio low input RNA Library Systems V2 (Nugen; 0507-08) according to the manufacturer's instructions by the NYU Genome Technology Center. Pooled libraries were sequenced as 50-nucleotide, paired-end reads on an Illumina HiSeq 2500 using v4 chemistry.

RNAseq data quality assessment and visualization

Illumina sequencing adapters and reads with Phred quality scores <20 were removed with Trimmomatic. Trimmed reads were mapped to the *Mus musculus* genome Ensembl annotation release 91 using STAR v2.5.3a with default settings. The number of reads uniquely mapping to each gene feature in the corresponding annotation file was determined using featureCounts. The resulting count tables were passed to R for further analyses. RNAseq data are deposited at the Gene Expression Omnibus repository under accession no. GSE126407.

Differential expression and gene ontology analyses

Consistency between replicates was checked using PCA and Euclidean distance–based hierarchical clustering on normalized counts. Weakly expressed genes, defined as having <2 fragment per kilobase of transcript per million mapped reads in at least one group of replicates, were removed from differential expression analysis. Counts normalization were performed using the method of trimmed mean of M-values from edgeR package. Differential expression analyses were performed using limma. Genes were considered significant when the observed log2 fold-change was >1 and the adjusted P value was <0.05. The set of significant genes for each contrast of interest was passed to Goseq for functional gene categories enrichment analyses.

Cell morphology

Sorted cells were spun onto Shandon Cytoslides with a Thermo Shandon Cytospin 4 cytofuge (10 min at 500 rpm), fixed with methanol; and stained with Wright-Giemsa (Sigma-Aldrich; GS500). Images were acquired in a Zeiss AxioObserver microscope using a magnification of 63× N.A. 1.4 in bright field at room temperature (RT). Zen software was used for image acquisition and ImageJ software, Fiji version 1.0 (National Institutes of Health), for contrast, brightness, and pseudo-color adjustments.

Confocal microscopy of WAT macrophages

WAT was stained as described (Martinez-Santibañez et al., 2014), with modifications. Mice were euthanized and slowly perfused by intracardiac injection with 20 ml of PBS/5 mM EDTA. Epididymal fat pads were excised and fixed for 1 h in PBS/1% PFA with gentle shaking at 4°C. After that, samples were blocked for 1 h in PBS/5% BSA (blocking buffer) with gentle rocking at RT. Primary antibodies were diluted in blocking buffer and added to fat samples for 18 h at 4°C. Samples were then washed three times with cold PBS and incubated with blocking buffer-diluted Bodipy (Thermo Fisher Scientific; D3922), Alexa Fluor 647–conjugated isolectin, Alexa Fluor 568–conjugated isolectin, and/or appropriate antibodies with gentle rocking at RT. Nuclei were stained with DAPI for 5 min at RT. Fat pads were imaged at RT on an inverted confocal microscope (Zeiss 710 MP; optical lenses 25× N.A. 0.8 and 63× N.A. 1.4 or a high-resolution Zeiss 880 with Airyscan fast; optical lenses 25× N.A. 0.8 and 63× N.A. 1.4) by placing the pad in Fluoromount-G (Southern Biotech; 0100-01) in a chambered coverslip. Zen software was used for image acquisition. ImageJ software, Fiji version 1.0, or Imaris/Bitplane software were used for contrast, brightness, and pseudo-color adjustments.

Adipo-Clear

Sample collection

The method was performed as described before (Chi et al., 2018). Mice were injected with 18 mg/kg of dextran-tetramethylrhodamine lysine fixable (Thermo Fisher Scientific; D1818). After 1 h, animals were anesthetized as described above, and an intracardiac perfusion/fixation was performed with 1× PBS followed by 4% PFA. All harvested samples were postfixed in 4% PFA at 4°C overnight. Fixed samples were washed in PBS for 1 h three times at RT.

Delipidation and permeabilization

Fixed samples were washed in 20, 40, 60, and 80% methanol in H_2O/0.1% Triton X-100/0.3 M glycine (B1N buffer, pH 7), and 100% methanol for 30 min each. Sample were then delipidated with 100% dichloromethane (DCM; Sigma-Aldrich) for 30 min three times. After delipidation, samples were washed in 100% methanol for 30 min twice, then in 80, 60, 40, and 20% methanol in B1N buffer for 30 min each step. All procedures above were performed at 4°C with shaking. Samples were then washed in B1N for 30 min twice followed by PBS/0.1% Triton X-100/0.05% Tween 20/2 µg/ml heparin (PTxwH buffer) for 1 h twice before further staining procedures.

Immunolabeling

Samples were incubated in primary antibody dilutions in PTxwH for 4 d. After primary antibody incubation, samples were washed in PTxwH for 5, 10, 15, and 30 min; 1, 2, and 4 h; and overnight, and then incubated in secondary antibody dilutions in PTxwH for 4 d. Samples were finally washed in PTwH for 5, 10, 15, and 30 min; 1, 2, and 4 h; and overnight.

Tissue clearing

Samples were embedded in 1% agarose in PBS and dehydrated in 25, 50, 75, and 100% methanol/H_2O series for 30 min at each step at RT. Following dehydration, samples were washed with 100% DCM for 30 min twice, followed by an overnight clearing step in dibenzyl ether (DBE; Sigma-Aldrich). Samples were stored at RT in the dark until imaging.

3D imaging

All whole-tissue samples were imaged on a light-sheet microscope (Ultramicroscope II; LaVision Biotec) equipped with 1.3× (used for whole-tissue views with low-magnification) and 4× objective lenses (used for high-magnification views) and an sCMOs camera (Andor Neo). Images were acquired with InspectorPro software (LaVision BioTec). Samples were placed in an imaging reservoir filled with DBE and illuminated from the side by the laser light sheet. The samples were scanned with the 488-, 640-, and 790-nm laser channels and with a step size of 3 µm for 1.3× objective and 2.5 µm for 4× objective.

Image processing

All whole-tissue images were generated using Imaris x64 software (version 8.0.1; Bitplane). 3D reconstruction was performed using the "volume rendering" function. Optical slices were obtained using the "orthoslicer" tool. Optical sections were generated using the "snapshot" tool.

Multiphoton microscopy

WT mice were anesthetized with i.p. injection of 20 µl/g of 2.5% Avertin before surgery for intravital imaging. Anesthesia was maintained by continuous administration of 1% isofluorane and 1 liter/min oxygen mixture while imaging was performed. Mice were injected with Hoechst dye (blue) and Qtracker 655 vascular labels for visualization of cell nuclei and blood vessels. qDots have a PEG surface coating specially designed to minimize interactions and do not get taken up by VAMs or any other cell type in the adipose tissue. 10 min following induction of anesthesia, mice were placed on a custom platform heated to 37°C. Upon loss of recoil to paw compression, a small incision was made in the abdomen. One perigonadal fat pad was located, exposed, and placed onto a raised block of thermal paste covered with a wetted wipe. A coverslip was placed on top of the fat. The platform was then transferred to the FV1000MPE Twin upright multiphoton system (Olympus) heated stage. Time-lapse was ±30 s with a total acquisition time between 15 min and 1 h depending on the condition. A complete Z stack (80 µm) was made during each acquisition. Depending on the experimental condition, 450 µg of dextran-rhodamine 70 kD was injected i.v. after 15 min of video acquisition.

Computational analysis of multiphoton microscopy

For each individual video, time-lapse was ±30 s with a total acquisition time varying from 15 min to 1 h. Raw data as imported from the microscope were used for all subsequent analyses. Imaris (Bitplane) software was used for preparation of individual images and videos. Some postanalysis pseudocolor adjustment was performed for individual images and videos to account for differences in autofluorescence and Hoechst labeling. For all comparison images and videos (comparing pseudo-color channels showing dextran-rhodamine labeling over time), identical settings for all image parameters were used.

Statistical analysis

Mean, SD, and SEM values were calculated with GraphPad Prism (GraphPad Software). Error bars represent ± SEM. Unpaired Student's t test was used to compare two variables. For three or more variables, one-way ANOVA was used with a Tukey post hoc test, as indicated in each figure legend. P values <0.05 were considered significant. Statistics symbols were *, $P < 0.05$; **, $P < 0.01$; and ***, $P < 0.001$.

Online supplemental material

Fig. S1 shows gating strategies and further flow cytometric and morphological analysis of the myeloid cells analyzed. Fig. S2 shows that VAMs present antigens captured from blood circulation to T cells. Fig. S3 shows additional analyses of animals fasted or treated with a β3 adrenergic receptor agonist. Fig. S4 shows further analyses of animals treated with LPS or infected with *S. aureus*. Video 1 shows the rapid uptake of blood-borne molecules by VAMs. Video 2 reveals the close association between VAMs and adipose tissue blood vessels. Video 3 shows that VAMs display lipid droplets in their cytoplasm. Video 4 shows an impaired uptake of rhodamine by macrophages from mice fed HFD.

Acknowledgments

We thank Drs. Carey Lumeng, Peter J. Murray, P'ng Locke, and Anthony W. Ferrante for helpful discussions at different stages of this project and Maria Lafaille for valuable comments on the manuscript. We thank the kind assistance of Dr. Michael Cammer in helping with microscope acquisitions and image processing. We thank Alireza Khodadadi-Jamayran from NYU Langone Medical Center Applied Bioinformatics Laboratory for initial assembly of processed RNAseq data. We thank Rita Chan for preparing bacteria cultures for injection. We thank Dr. Gabriel Victora for kindly allowing the use of the FV1000MPE Twin upright multiphoton system (Olympus). We thank Dr. Dan Littman for generously sharing equipment, and critical review of the manuscript.

The NYU microscope core is supported by the National Center for Research Resources, grant S10 RR023704-01A1. NYU genomic core is a shared resource partially supported by the Laura and Isaac Perlmutter Cancer Center, Cancer Center Support Grant P30CA016087. H.M. Silva was supported by a fellowship from the National Council for Scientific and Technological Development and a postdoctoral fellowship from Dr. Bernard B. Levine. A. Báfica, G.F. Rodrigues-Luiz, D. Mucida, and D.S. Mansur were funded by the Computational Biology Program, Coordenação de Aperfeiçoamento de Pessoal de Nível Superior.

The authors declare no competing financial interests.

Author contributions: H.M. Silva, A. Báfica, and J.J. Lafaille conceived the study; H.M. Silva and A. Báfica supervised the study; H.M. Silva, A. Báfica, D. Mucida, and J.J. Lafaille designed experiments; H.M. Silva, A. Báfica, P.d.A. Santos, R.D.N. Arifa, and D.A.G.B. Mendes performed and analyzed experiments; J. Chi, A. Crane, and P. Cohen set up, performed, and analyzed adipo clear experiments; P. Martin, K. Cadwell, and V.J. Torres

provided bacterial reagents and expertise; D.P. Hoytema van Konijnenburg and B.S. Reis helped set up adipose tissue in vivo imaging experiments; G.F. Rodrigues-Luiz and D.S. Mansur were responsible for RNAseq data analysis; H.M. Silva prepared figures; and J.J. Lafaille, H.M. Silva, and D. Mucida wrote the paper.

Submitted: 4 June 2018
Revised: 10 December 2018
Accepted: 19 February 2019

References

A-Gonzalez, N., J.A. Quintana, S. García-Silva, M. Mazariegos, A. González de la Aleja, J.A. Nicolás-Ávila, W. Walter, J.M. Adrover, G. Crainiciuc, V.K. Kuchroo, et al. 2017. Phagocytosis imprints heterogeneity in tissue-resident macrophages. *J. Exp. Med.* 214:1281–1296. https://doi.org/10.1084/jem.20161375

Ajami, B., J.L. Bennett, C. Krieger, W. Tetzlaff, and F.M. Rossi. 2007. Local self-renewal can sustain CNS microglia maintenance and function throughout adult life. *Nat. Neurosci.* 10:1538–1543. https://doi.org/10.1038/nn2014

Alemán, J.O., N.M. Iyengar, J.M. Walker, G.L. Milne, J.C. Da Rosa, Y. Liang, D. D. Giri, X.K. Zhou, M.N. Pollak, C.A. Hudis, et al. 2017. Effects of Rapid Weight Loss on Systemic and Adipose Tissue Inflammation and Metabolism in Obese Postmenopausal Women. *J Endocr Soc.* 1:625–637. https://doi.org/10.1210/js.2017-00020

Amano, S.U., J.L. Cohen, P. Vangala, M. Tencerova, S.M. Nicoloro, J.C. Yawe, Y. Shen, M.P. Czech, and M. Aouadi. 2014. Local proliferation of macrophages contributes to obesity-associated adipose tissue inflammation. *Cell Metab.* 19:162–171. https://doi.org/10.1016/j.cmet.2013.11.017

Aouadi, M., P. Vangala, J.C. Yawe, M. Tencerova, S.M. Nicoloro, J.L. Cohen, Y. Shen, and M.P. Czech. 2014. Lipid storage by adipose tissue macrophages regulates systemic glucose tolerance. *Am. J. Physiol. Endocrinol. Metab.* 307:E374–E383. https://doi.org/10.1152/ajpendo.00187.2014

Arch, J.R. 2008. The discovery of drugs for obesity, the metabolic effects of leptin and variable receptor pharmacology: perspectives from beta3-adrenoceptor agonists. *Naunyn Schmiedebergs Arch. Pharmacol.* 378:225–240. https://doi.org/10.1007/s00210-008-0271-1

Bartness, T.J., Y. Liu, Y.B. Shrestha, and V. Ryu. 2014. Neural innervation of white adipose tissue and the control of lipolysis. *Front. Neuroendocrinol.* 35:473–493. https://doi.org/10.1016/j.yfrne.2014.04.001

Bingisser, R., C. Stey, M. Weller, P. Groscurth, E. Russi, and K. Frei. 1996. Apoptosis in human alveolar macrophages is induced by endotoxin and is modulated by cytokines. *Am. J. Respir. Cell Mol. Biol.* 15:64–70. https://doi.org/10.1165/ajrcmb.15.1.8679223

Boulenouar, S., X. Michelet, D. Duquette, D. Alvarez, A.E. Hogan, C. Dold, D. O'Connor, S. Stutte, A. Tavakkoli, D. Winters, et al. 2017. Adipose Type One Innate Lymphoid Cells Regulate Macrophage Homeostasis through Targeted Cytotoxicity. *Immunity.* 46:273–286. https://doi.org/10.1016/j.immuni.2017.01.008

Carbone, R., S. Fré, G. Iannolo, F. Belleudi, P. Mancini, P.G. Pelicci, M.R. Torrisi, and P.P. Di Fiore. 1997. eps15 and eps15R are essential components of the endocytic pathway. *Cancer Res.* 57:5498–5504.

Chi, J., Z. Wu, C.H.J. Choi, L. Nguyen, S. Tegegne, S.E. Ackerman, A. Crane, F. Marchildon, M. Tessier-Lavigne, and P. Cohen. 2018. Three-Dimensional Adipose Tissue Imaging Reveals Regional Variation in Beige Fat Biogenesis and PRDM16-Dependent Sympathetic Neurite Density. *Cell Metab.* 27:226–236.e3. https://doi.org/10.1016/j.cmet.2017.12.011

Chorro, L., A. Sarde, M. Li, K.J. Woollard, P. Chambon, B. Malissen, A. Kissenpfennig, J.B. Barbaroux, R. Groves, and F. Geissmann. 2009. Langerhans cell (LC) proliferation mediates neonatal development, homeostasis, and inflammation-associated expansion of the epidermal LC network. *J. Exp. Med.* 206:3089–3100. https://doi.org/10.1084/jem.20091586

Cinti, S., G. Mitchell, G. Barbatelli, I. Murano, E. Ceresi, E. Faloia, S. Wang, M. Fortier, A.S. Greenberg, and M.S. Obin. 2005. Adipocyte death defines macrophage localization and function in adipose tissue of obese mice and humans. *J. Lipid Res.* 46:2347–2355. https://doi.org/10.1194/jlr.M500294-JLR200

Coats, B.R., K.Q. Schoenfelt, V.C. Barbosa-Lorenzi, E. Peris, C. Cui, A. Hoffman, G. Zhou, S. Fernandez, L. Zhai, B.A. Hall, et al. 2017. Metabolically Activated Adipose Tissue Macrophages Perform Detrimental and Beneficial Functions during Diet-Induced Obesity. *Cell Reports.* 20:3149–3161. https://doi.org/10.1016/j.celrep.2017.08.096

Cypess, A.M., L.S. Weiner, C. Roberts-Toler, E. Franquet Elía, S.H. Kessler, P. A. Kahn, J. English, K. Chatman, S.A. Trauger, A. Doria, and G.M. Kolodny. 2015. Activation of human brown adipose tissue by a β3-adrenergic receptor agonist. *Cell Metab.* 21:33–38. https://doi.org/10.1016/j.cmet.2014.12.009

Dalmas, E., K. Clément, and M. Guerre-Millo. 2011. Defining macrophage phenotype and function in adipose tissue. *Trends Immunol.* 32:307–314. https://doi.org/10.1016/j.it.2011.04.008

Duncan, R.E., M. Ahmadian, K. Jaworski, E. Sarkadi-Nagy, and H.S. Sul. 2007. Regulation of lipolysis in adipocytes. *Annu. Rev. Nutr.* 27:79–101. https://doi.org/10.1146/annurev.nutr.27.061406.093734

Feinstein, R., H. Kanety, M.Z. Papa, B. Lunenfeld, and A. Karasik. 1993. Tumor necrosis factor-alpha suppresses insulin-induced tyrosine phosphorylation of insulin receptor and its substrates. *J. Biol. Chem.* 268:26055–26058.

Fischer-Posovszky, P., Q.A. Wang, I.W. Asterholm, J.M. Rutkowski, and P.E. Scherer. 2011. Targeted deletion of adipocytes by apoptosis leads to adipose tissue recruitment of alternatively activated M2 macrophages. *Endocrinology.* 152:3074–3081. https://doi.org/10.1210/en.2011-1031

Fitzgibbons, T.P., and M.P. Czech. 2016. Emerging evidence for beneficial macrophage functions in atherosclerosis and obesity-induced insulin resistance. *J. Mol. Med. (Berl.).* 94:267–275. https://doi.org/10.1007/s00109-016-1385-4

Ginhoux, F., and M. Guilliams. 2016. Tissue-Resident Macrophage Ontogeny and Homeostasis. *Immunity.* 44:439–449. https://doi.org/10.1016/j.immuni.2016.02.024

Ginhoux, F., M. Greter, M. Leboeuf, S. Nandi, P. See, S. Gokhan, M.F. Mehler, S.J. Conway, L.G. Ng, E.R. Stanley, et al. 2010. Fate mapping analysis reveals that adult microglia derive from primitive macrophages. *Science.* 330:841–845. https://doi.org/10.1126/science.1194637

Hilbi, H., Y. Chen, K. Thirumalai, and A. Zychlinsky. 1997. The interleukin 1beta-converting enzyme, caspase 1, is activated during Shigella flexneri-induced apoptosis in human monocyte-derived macrophages. *Infect. Immun.* 65:5165–5170.

Hill, D.A., H.W. Lim, Y.H. Kim, W.Y. Ho, Y.H. Foong, V.L. Nelson, H.C.B. Nguyen, K. Chegireddy, J. Kim, A. Habertheuer, et al. 2018. Distinct macrophage populations direct inflammatory versus physiological changes in adipose tissue. *Proc. Natl. Acad. Sci. USA.* 115:E5096–E5105. https://doi.org/10.1073/pnas.1802611115

Hotamisligil, G.S., N.S. Shargill, and B.M. Spiegelman. 1993. Adipose expression of tumor necrosis factor-alpha: direct role in obesity-linked insulin resistance. *Science.* 259:87–91. https://doi.org/10.1126/science.7678183

Hotamisligil, G.S., P. Arner, J.F. Caro, R.L. Atkinson, and B.M. Spiegelman. 1995. Increased adipose tissue expression of tumor necrosis factor-alpha in human obesity and insulin resistance. *J. Clin. Invest.* 95:2409–2415. https://doi.org/10.1172/JCI117936

Kazak, L., E.T. Chouchani, G.Z. Lu, M.P. Jedrychowski, C.J. Bare, A.I. Mina, M. Kumari, S. Zhang, I. Vuckovic, D. Laznik-Bogoslavski, et al. 2017. Genetic Depletion of Adipocyte Creatine Metabolism Inhibits Diet-Induced Thermogenesis and Drives Obesity. *Cell Metab.* 26:660–671.e3. https://doi.org/10.1016/j.cmet.2017.08.009

Kim, J.I., J.Y. Huh, J.H. Sohn, S.S. Choe, Y.S. Lee, C.Y. Lim, A. Jo, S.B. Park, W. Han, and J.B. Kim. 2015. Lipid-overloaded enlarged adipocytes provoke insulin resistance independent of inflammation. *Mol. Cell. Biol.* 35:1686–1699. https://doi.org/10.1128/MCB.01321-14

Kosteli, A., E. Sugaru, G. Haemmerle, J.F. Martin, J. Lei, R. Zechner, and A.W. Ferrante Jr. 2010. Weight loss and lipolysis promote a dynamic immune response in murine adipose tissue. *J. Clin. Invest.* 120:3466–3479. https://doi.org/10.1172/JCI42845

Kratz, M., B.R. Coats, K.B. Hisert, D. Hagman, V. Mutskov, E. Peris, K.Q. Schoenfelt, J.N. Kuzma, I. Larson, P.S. Billing, et al. 2014. Metabolic dysfunction drives a mechanistically distinct proinflammatory phenotype in adipose tissue macrophages. *Cell Metab.* 20:614–625. https://doi.org/10.1016/j.cmet.2014.08.010

Krawczyk, C.M., T. Holowka, J. Sun, J. Blagih, E. Amiel, R.J. DeBerardinis, J.R. Cross, E. Jung, C.B. Thompson, R.G. Jones, and E.J. Pearce. 2010. Toll-like receptor-induced changes in glycolytic metabolism regulate dendritic cell activation. *Blood.* 115:4742–4749. https://doi.org/10.1182/blood-2009-10-249540

Kvainickas, A., A. Jimenez-Orgaz, H. Nägele, Z. Hu, J. Dengjel, and F. Steinberg. 2017. Cargo-selective SNX-BAR proteins mediate retromer trimer independent retrograde transport. *J. Cell Biol.* 216:3677–3693. https://doi.org/10.1083/jcb.201702137

Lee, J., H.G. Remold, M.H. Ieong, and H. Kornfeld. 2006. Macrophage apoptosis in response to high intracellular burden of Mycobacterium tuberculosis is mediated by a novel caspase-independent pathway. *J. Immunol.* 176:4267–4274. https://doi.org/10.4049/jimmunol.176.7.4267

Li, P., Z. Zhu, Y. Lu, and J.G. Granneman. 2005. Metabolic and cellular plasticity in white adipose tissue II: role of peroxisome proliferator-activated receptor-alpha. *Am. J. Physiol. Endocrinol. Metab.* 289: E617–E626. https://doi.org/10.1152/ajpendo.00010.2005

Lim, J.P., P. Gosavi, J.D. Mintern, E.M. Ross, and P.A. Gleeson. 2015. Sorting nexin 5 selectively regulates dorsal-ruffle-mediated macropinocytosis in primary macrophages. *J. Cell Sci.* 128:4407–4419. https://doi.org/10.1242/jcs.174359

Lumeng, C.N. 2013. Innate immune activation in obesity. *Mol. Aspects Med.* 34: 12–29. https://doi.org/10.1016/j.mam.2012.10.002

Lumeng, C.N., J.L. Bodzin, and A.R. Saltiel. 2007. Obesity induces a phenotypic switch in adipose tissue macrophage polarization. *J. Clin. Invest.* 117:175–184. https://doi.org/10.1172/JCI29881

Malik, M., E.M. van Gelderen, J.H. Lee, D.L. Kowalski, M. Yen, R. Goldwater, S.K. Mujais, M.P. Schaddelee, P. de Koning, A. Kaibara, et al. 2012. Proarrhythmic safety of repeat doses of mirabegron in healthy subjects: a randomized, double-blind, placebo-, and active-controlled thorough QT study. *Clin. Pharmacol. Ther.* 92:696–706. https://doi.org/10.1038/clpt.2012.181

Martinez-Santibañez, G., K.W. Cho, and C.N. Lumeng. 2014. Imaging white adipose tissue with confocal microscopy. *Methods Enzymol.* 537:17–30. https://doi.org/10.1016/B978-0-12-411619-1.00002-1

Merad, M., M.G. Manz, H. Karsunky, A. Wagers, W. Peters, I. Charo, I.L. Weissman, J.G. Cyster, and E.G. Engleman. 2002. Langerhans cells renew in the skin throughout life under steady-state conditions. *Nat. Immunol.* 3:1135–1141. https://doi.org/10.1038/ni852

Mildner, A., J. Schönheit, A. Giladi, E. David, D. Lara-Astiaso, E. Lorenzo-Vivas, F. Paul, L. Chappell-Maor, J. Priller, A. Leutz, et al. 2017. Genomic Characterization of Murine Monocytes Reveals C/EBPβ Transcription Factor Dependence of $Ly6C^-$ Cells. *Immunity.* 46:849–862.e7. https://doi.org/10.1016/j.immuni.2017.04.018

Mottillo, E.P., X.J. Shen, and J.G. Granneman. 2007. Role of hormone-sensitive lipase in beta-adrenergic remodeling of white adipose tissue. *Am. J. Physiol. Endocrinol. Metab.* 293:E1188–E1197. https://doi.org/10.1152/ajpendo.00051.2007

Nguyen, M.T., S. Favelyukis, A.K. Nguyen, D. Reichart, P.A. Scott, A. Jenn, R. Liu-Bryan, C.K. Glass, J.G. Neels, and J.M. Olefsky. 2007. A subpopulation of macrophages infiltrates hypertrophic adipose tissue and is activated by free fatty acids via Toll-like receptors 2 and 4 and JNK-dependent pathways. *J. Biol. Chem.* 282:35279–35292. https://doi.org/10.1074/jbc.M706762200

O'Neill, L.A., and D.G. Hardie. 2013. Metabolism of inflammation limited by AMPK and pseudo-starvation. *Nature.* 493:346–355. https://doi.org/10.1038/nature11862

O'Sullivan, M.P., S. O'Leary, D.M. Kelly, and J. Keane. 2007. A caspase-independent pathway mediates macrophage cell death in response to Mycobacterium tuberculosis infection. *Infect. Immun.* 75:1984–1993. https://doi.org/10.1128/IAI.01107-06

Palsson-McDermott, E.M., A.M. Curtis, G. Goel, M.A. Lauterbach, F.J. Sheedy, L.E. Gleeson, M.W. van den Bosch, S.R. Quinn, R. Domingo-Fernandez, D.G. Johnston, et al. 2015. Pyruvate kinase M2 regulates Hif-1α activity and IL-1β induction and is a critical determinant of the warburg effect in LPS-activated macrophages. *Cell Metab.* 21:65–80. https://doi.org/10.1016/j.cmet.2014.12.005

Parkhurst, C.N., G. Yang, I. Ninan, J.N. Savas, J.R. Yates III, J.J. Lafaille, B.L. Hempstead, D.R. Littman, and W.B. Gan. 2013. Microglia promote learning-dependent synapse formation through brain-derived neurotrophic factor. *Cell.* 155:1596–1609. https://doi.org/10.1016/j.cell.2013.11.030

Rebuffé-Scrive, M., R. Surwit, M. Feinglos, C. Kuhn, and J. Rodin. 1993. Regional fat distribution and metabolism in a new mouse model (C57BL/6J) of non-insulin-dependent diabetes mellitus. *Metabolism.* 42: 1405–1409. https://doi.org/10.1016/0026-0495(93)90190-Y

Rutkowski, J.M., J.H. Stern, and P.E. Scherer. 2015. The cell biology of fat expansion. *J. Cell Biol.* 208:501–512. https://doi.org/10.1083/jcb.201409063

Schulz, C., E. Gomez Perdiguero, L. Chorro, H. Szabo-Rogers, N. Cagnard, K. Kierdorf, M. Prinz, B. Wu, S.E. Jacobsen, J.W. Pollard, et al. 2012. A lineage of myeloid cells independent of Myb and hematopoietic stem cells. *Science.* 336:86–90. https://doi.org/10.1126/science.1219179

Sharma, A.M. 2002. Adipose tissue: a mediator of cardiovascular risk. *Int. J. Obes. Relat. Metab. Disord.* 26(S4, Suppl 4):S5–S7. https://doi.org/10.1038/sj.ijo.0802210

Shaul, M.E., G. Bennett, K.J. Strissel, A.S. Greenberg, and M.S. Obin. 2010. Dynamic, M2-like remodeling phenotypes of CD11c+ adipose tissue macrophages during high-fat diet--induced obesity in mice. *Diabetes.* 59:1171–1181. https://doi.org/10.2337/db09-1402

Sigismund, S., T. Woelk, C. Puri, E. Maspero, C. Tacchetti, P. Transidico, P.P. Di Fiore, and S. Polo. 2005. Clathrin-independent endocytosis of ubiquitinated cargos. *Proc. Natl. Acad. Sci. USA.* 102:2760–2765. https://doi.org/10.1073/pnas.0409817102

Simonetti, B., C.M. Danson, K.J. Heesom, and P.J. Cullen. 2017. Sequence-dependent cargo recognition by SNX-BARs mediates retromer-independent transport of CI-MPR. *J. Cell Biol.* 216:3695–3712. https://doi.org/10.1083/jcb.201703015

Singh, R., and A.M. Cuervo. 2012. Lipophagy: connecting autophagy and lipid metabolism. *Int. J. Cell Biol.* 2012:282041. https://doi.org/10.1155/2012/282041

Sun, K., C.M. Kusminski, and P.E. Scherer. 2011. Adipose tissue remodeling and obesity. *J. Clin. Invest.* 121:2094–2101. https://doi.org/10.1172/JCI45887

Surwit, R.S., C.M. Kuhn, C. Cochrane, J.A. McCubbin, and M.N. Feinglos. 1988. Diet-induced type II diabetes in C57BL/6J mice. *Diabetes.* 37: 1163–1167. https://doi.org/10.2337/diab.37.9.1163

Takasu, T., M. Ukai, S. Sato, T. Matsui, I. Nagase, T. Maruyama, M. Sasamata, K. Miyata, H. Uchida, and O. Yamaguchi. 2007. Effect of (R)-2-(2-aminothiazol-4-yl)-4′-{2-[(2-hydroxy-2-phenylethyl)amino]ethyl} acetanilide (YM178), a novel selective beta3-adrenoceptor agonist, on bladder function. *J. Pharmacol. Exp. Ther.* 321:642–647. https://doi.org/10.1124/jpet.106.115840

von Eyben, F.E., E. Mouritsen, J. Holm, P. Montvilas, G. Dimcevski, G. Suciu, I. Helleberg, L. Kristensen, and R. von Eyben. 2003. Intra-abdominal obesity and metabolic risk factors: a study of young adults. *Int. J. Obes. Relat. Metab. Disord.* 27:941–949. https://doi.org/10.1038/sj.ijo.0802309

Wang, A., S.C. Huen, H.H. Luan, S. Yu, C. Zhang, J.D. Gallezot, C.J. Booth, and R. Medzhitov. 2016. Opposing effects of fasting metabolism on tissue tolerance in bacterial and viral inflammation. *Cell.* 166:1512–1525.e12. https://doi.org/10.1016/j.cell.2016.07.026

Watanabe, S., and E. Boucrot. 2017. Fast and ultrafast endocytosis. *Curr. Opin. Cell Biol.* 47:64–71. https://doi.org/10.1016/j.ceb.2017.02.013

Weisberg, S.P., D. McCann, M. Desai, M. Rosenbaum, R.L. Leibel, and A.W. Ferrante Jr. 2003. Obesity is associated with macrophage accumulation in adipose tissue. *J. Clin. Invest.* 112:1796–1808. https://doi.org/10.1172/JCI200319246

Weiss, J.M., A.M. Bilate, M. Gobert, Y. Ding, M.A. Curotto de Lafaille, C.N. Parkhurst, H. Xiong, J. Dolpady, A.B. Frey, M.G. Ruocco, et al. 2012. Neuropilin 1 is expressed on thymus-derived natural regulatory T cells, but not mucosa-generated induced Foxp3+ T reg cells. *J. Exp. Med.* 209: 1723–1742: S1. https://doi.org/10.1084/jem.20120914

Wentworth, J.M., G. Naselli, W.A. Brown, L. Doyle, B. Phipson, G.K. Smyth, M. Wabitsch, P.E. O'Brien, and L.C. Harrison. 2010. Pro-inflammatory CD11c+CD206+ adipose tissue macrophages are associated with insulin resistance in human obesity. *Diabetes.* 59:1648–1656. https://doi.org/10.2337/db09-0287

Wolf, Y., S. Boura-Halfon, N. Cortese, Z. Haimon, H. Sar Shalom, Y. Kuperman, V. Kalchenko, A. Brandis, E. David, Y. Segal-Hayoun, et al. 2017. Brown-adipose-tissue macrophages control tissue innervation and homeostatic energy expenditure. *Nat. Immunol.* 18:665–674. https://doi.org/10.1038/ni.3746

Wynn, T.A., A. Chawla, and J.W. Pollard. 2013. Macrophage biology in development, homeostasis and disease. *Nature.* 496:445–455. https://doi.org/10.1038/nature12034

Xaus, J., M. Comalada, A.F. Valledor, J. Lloberas, F. López-Soriano, J.M. Argilés, C. Bogdan, and A. Celada. 2000. LPS induces apoptosis in macrophages mostly through the autocrine production of TNF-alpha. *Blood.* 95:3823–3831.

Xu, H., G.T. Barnes, Q. Yang, G. Tan, D. Yang, C.J. Chou, J. Sole, A. Nichols, J.S. Ross, L.A. Tartaglia, and H. Chen. 2003. Chronic inflammation in fat plays a crucial role in the development of obesity-related insulin resistance. *J. Clin. Invest.* 112:1821–1830. https://doi.org/10.1172/JCI200319451

Xu, X., A. Grijalva, A. Skowronski, M. van Eijk, M.J. Serlie, and A.W. Ferrante Jr. 2013. Obesity activates a program of lysosomal-dependent lipid metabolism in adipose tissue macrophages independently of classic activation. *Cell Metab.* 18:816–830. https://doi.org/10.1016/j.cmet.2013.11.001

Yoshida, T., N. Sakane, Y. Wakabayashi, T. Umekawa, and M. Kondo. 1994. Anti-obesity and anti-diabetic effects of CL 316,243, a highly specific beta 3-adrenoceptor agonist, in yellow KK mice. *Life Sci.* 54:491–498. https://doi.org/10.1016/0024-3205(94)00408-0

Yu, H.B., M.A. Croxen, A.M. Marchiando, R.B. Ferreira, K. Cadwell, L.J. Foster, and B.B. Finlay. 2014. Autophagy facilitates Salmonella replication in HeLa cells. *MBio.* 5:e00865–e14. https://doi.org/10.1128/mBio.00865-14

Zechner, R., P.C. Kienesberger, G. Haemmerle, R. Zimmermann, and A. Lass. 2009. Adipose triglyceride lipase and the lipolytic catabolism of cellular fat stores. *J. Lipid Res.* 50:3–21. https://doi.org/10.1194/jlr.R800031-JLR200

Zeyda, M., K. Gollinger, E. Kriehuber, F.W. Kiefer, A. Neuhofer, and T.M. Stulnig. 2010. Newly identified adipose tissue macrophage populations in obesity with distinct chemokine and chemokine receptor expression. *Int. J. Obes.* 34:1684–1694. https://doi.org/10.1038/ijo.2010.103